EVALUATION OF INSTANTANEOUS PRESSURE MEASUREMENTS ON A ROD SURFACE IN A 5 X 5 BUNDLE AND VALIDATION THROUGH CFD

A Thesis

by

NATALIE CHRISTINE GALEGAR

Submitted to the Office of Graduate and Professional Studies of
Texas A&M University
in partial fulfillment of the requirements for the degree of

MASTER OF SCIENCE

Chair of Committee,	Yassin A. Hassan
Committee Members,	William H. Marlow
	Maria D. King
Head of Department,	Yassin A. Hassan

May 2015

Major Subject: Nuclear Engineering

ABSTRACT

Grid-To-Rod-Fretting (GTRF) in PWR fuel assemblies is a major issue of concern to vendors and utilities. Instantaneous pressure fluctuations on a fuel rod surface can help characterize the GTRF potential within a fuel bundle. As part of a collaboration with Westinghouse Electric Company, instantaneous pressure was collected experimentally at Texas A&M using pressure transducers installed within an instrumented rod. In addition, a Computational Fluid Dynamics (CFD) simulation was generated at the Westinghouse Fuel Fabrication Facility in Columbia, SC using a uniform velocity inlet condition. The simulation was repeated at Texas A&M with a non-uniform velocity inlet condition to determine the validity of the uniform inlet velocity assumption. The results from both simulations were used to compare with the experimental measurements.

Instantaneous pressure obtained from CFD agreed with the experimental data within 10%. The trend of the pressure evolution along the axial direction showed a maximum increase at 1.4 hydraulic diameters from the grid. Measurements and simulation results were compared at 5 different azimuthal orientations and 8 axial elevations. Further testing and more robust simulations will be needed to determine if the two results could agree with less than 10% difference.

Through this analysis, it was discovered that the non-uniform inlet velocity condition yields different results than the constant velocity condition. On average, both simulations produced the theoretically expected number of vortices per subchannel,

however, more cross flow was observed in non-uniform velocity inlet simulation throughout the axial domain than the first simulation. In this study, the flow appears to retain memory of the inlet boundary condition well after the turbulent effects from the mixing vanes begin to dissipate. This implies that defining the inlet velocity properly is vital for this type of problem.

Additionally, velocity vectors from the two CFD simulations were reduced to the resolution of experimental PIV measurements. The purpose was to prove that reducing vector field resolution does not lose meaningful data. Through side-by-side comparison, it was determined that this process does not remove the pertinent flow structures and will provide a means to benchmark PIV results to CFD using the same resolution.

DEDICATION

This work is dedicated to the love of my life and future husband, William, and my parents, whose love and support has made this work possible.

ACKNOWLEDGEMENTS

I would like to thank my committee chair, Dr. Hassan who guided and funded my research, and my committee members, Dr. Marlow, and Dr. King, for their support throughout the course of this research.

Thanks to Dr. Elvis Dominguez whose guidance and support made this work possible and to Michael Conner and Roger Lu of Westinghouse who provided industry guidance and direction during the course of this research.

Additionally, I would like to thank the Texas A&M Supercomputing Facility for the use of the ADA supercomputer. This access greatly reduced the time needed to run my simulations.

Finally, thanks to my fiancé for his patience and love and to my parents for their encouragement over the years.

NOMENCLATURE

GTRF	Grid-to-Rod-Fretting
PWR	Pressurized Water Reactor
FIV	Flow Induced Vibration
CFD	Computational Fluid Dynamics
LES	Large Eddy Simulation
PIV	Particle Image Velocimetry
S1	Simulation 1
S2	Simulation 2
RST	Reynolds Stress Turbulence Model
RANS	Reynolds-Averaged Navier-Stokes
PTV	Particle Tracking Algorithm
Dh	Hydraulic Diameter

TABLE OF CONTENTS

Page

LIST OF FIGURES

Page

LIST OF TABLES

Page

1. INTRODUCTION AND LITERATURE REVIEW

Grid-to-rod-fretting (GTRF) is a problem that continues to cause fuel failure in Pressurized Water Reactors (PWR). As coolant water flows through fuel assemblies at high velocities, it vibrates the fuel rods, which are held in place by structural grids. When the rods vibrate, they rub against the contact points in the grid, which can cause the rod to rupture and the cladding to fail. Fuel rod failures cost nuclear power utilities millions of dollars in preventative measures and cleanup, leading to a push for manufacturers to produce 100% leak-free fuel. The goal of this work is to characterize instantaneous pressures and velocities on the fuel rod surface that could lead to fuel failure.

As explained by Park et al. [1], nuclear manufacturers are working to create fuel that is resistant to fretting wear by improving the manufacturing process and the fuel design. Even with design improvements, fretting-related failures still remain. In addition to fretting wear, rod vibration is a concern because it increased the departure from nucleate boiling margin. While fuel design, fabrication, and reactor operation contribute to the intensity and probability of fuel failure, they are not the only factors. Kim [2] points out that a lack of positive grid-to-rod contact force in combination with excessive flow-induced vibration (FIV) will cause fretting wear fuel failure. Pettigrew et al. [3] explains that the elimination of fretting wear will be a balancing act. Minimum structural support is sometimes preferred in order to reduce pressure drop and improve neutron

economy, but this lack of support combined with high flow velocities can lead to higher FIV.

Computational Fluid Dynamics (CFD) is becoming an important tool to gain insight into GTRF. However, since nuclear rod bundles with spacer grids pose such complicated problem for CFD, it is still important to benchmark computational results with experimental data. For instance, Horvath and Dressel [4] were concerned with determining the optimal turbulence model and mesh to achieve numerical results comparable to experimental data. The purpose of this work was to set the groundwork for accurate numerical simulation of more complex geometries in the future. Liu et al. [5] was similarly interested in ascertaining mesh, boundary conditions, wall treatment, and the appropriate turbulence model that produces a closer comparison to experimental results. This work centered on numerically describing the complex swirl pattern present in rod bundle flow. In Podila et al. [6], a CFD study was performed using a 5x5 rod bundle with a split-type spacer grid to directly compare velocity and vorticity results to experimental data collected by KAERI. Here, the goal was to develop a simulation that could adequately simulate single and two phase flow in nuclear rod bundles. A brief overview of the work performed relating to CFD modeling of fretting wear and benchmarking CFD results to experimental data is presented here.

Hatman et al. [7] used the STAR-CCM+ CFD code to determine the velocity distribution at the periphery of the bottom and top spans, where fretting-wear typically occurs. A quarter of the reactor was modeled from the lower plenum to the upper plenum using steady state physics. The conclusion called for an additional transient

study to capture the unsteady forces acting on the fuel rods. In a study by Elmahdi et al. [8], it is pointed out that while hydraulic testing is important in order to understand rod vibration and fretting, only CFD can provide complete resolution of forces acting on the fuel rods. Here, the author uses a large eddy simulation (LES) of a simplified smaller geometry to study the vibration forces on a fuel rod. The 3x3 bundle geometry used in this work is representative of a 17x17 fuel design. Bakosi et al. [9] demonstrated that LES simulations of 3x3 and 5x5 rod bundles were a viable option for calculating excitation forces that provide knowledge about GTRF. Here, the goal was to reproduce results of Elmahdi et al. [8] using Hydra-TH instead of STAR-CCM+. The work of Ikeno and Kajishima [10] involved investigation of the swirl decay downstream of a spacer grid using LES. This was performed using a 3x2 geometry with immersed boundary conditions and dynamic SGS model to treat the complex geometry. Delafontaine and Ricciardi [11] used a STAR-CCM+ LES run to determine the fluctuating fluid forces that act on rods downstream of mixing vanes. In this work, a 4 subchannel model was used to study pressure and shear forces every 45 degrees around the central rod. Downstream of the grid, periodic boundary conditions were set to reproduce the cross-flow effect from neighboring subchannels. Moussou et al. [12] took a slightly different approach, comparing the unsteady loading results of a 4 subchannel model to classical correlation results. In this work, LES was used to calculate the unsteady forces and a periodic boundary condition was applied to simulate the flow interaction from neighboring subchannels.

In Chang et al. [13], 2D Laser Doppler Anemometry (LDA) experimental data was collected on a 5x5 rod bundle. The goal of this study was to provide experimental data that could be used to validate computational results. Dominguez-Ontiveros et al. [14] presents experimental Particle Image Velocimetry (PIV) data and discusses how it can be used as a benchmark for a 5x5 CFD results. The work by Kim et al. [15] explains that CFD codes are useful tools to collect data since it is difficult to measure flow induced forces in actual reactors. Here it mentions that CFD results are affected by the turbulence models and wall functions selected and therefore should be verified with experimental data. In Conner et al. [16], a 5x5 single-phase STAR-CD model was compared to experimental PIV data to create a benchmarking methodology. Here it mentions that STAR-CD was used because it creates high quality meshes, contains accurate numerical schemes, and the turbulence models contained within the code yield results comparable to benchmark data. Conner et al. [17] reproduced the same comparison as Conner et al. [16] with updated experimental data. The PIV data collected in this study was performed using a different hydraulic loop and newer PIV technology. Here it explains that predicting downstream flow fields with CFD requires good benchmarking data.

Advances in computer technology have generated more enthusiasm for CFD modeling over experiments. With increased speed and memory, nuclear fuel geometries have expanded from the 2 and 4 subchannel geometries to 5x5 rod bundle geometries. As CFD models become closer and closer to realistic reactor conditions, there is still a need to benchmark with any available experimental results. The purpose of this work is

to validate experimental data with LES results as well as understand fluctuating instantaneous pressure on a fuel rod surface downstream of a mixing grid. The geometry used in this study is a 5x5 rod bundle similar to the geometry analyzed in Yan et al. [18].

The remainder of this paper will be organized as follows. Section 2 will discuss the experimental data collection, and analysis, as well as the CFD setup and analysis.

2. EXPERIMENTAL APPARATUS

The following is a combination of the experimental facility and methodology used to collect the experimental data that was analyzed in this work.

2.1 Experimental Test Facility

The experiments for this project were performed at the Optical Multi-phase Flow Research Laboratory operated by the Nuclear Engineering Department at Texas A&M University. A detailed description of the Texas A&M experimental hydraulic loop is provided in of Reference 14 and a picture of the full loop is given in Figure 1. Additionally, close-up pictures of the inlet and outlet plenums are provided in Figure 2 and Figure 3 respectively. The loop is a closed, isothermal, room temperature, hydraulic test loop designed to provide pressure and velocity test data using sensors and optics respectively. The loop was funded by Westinghouse to study and measure key hydraulic parameters in a 5x5 rod bundle with mixing grids. A technical objective of this experimental loop is to obtain new types of data using state-of-the-art measurement techniques.

Figure 1: Texas A&M hydraulic loop.

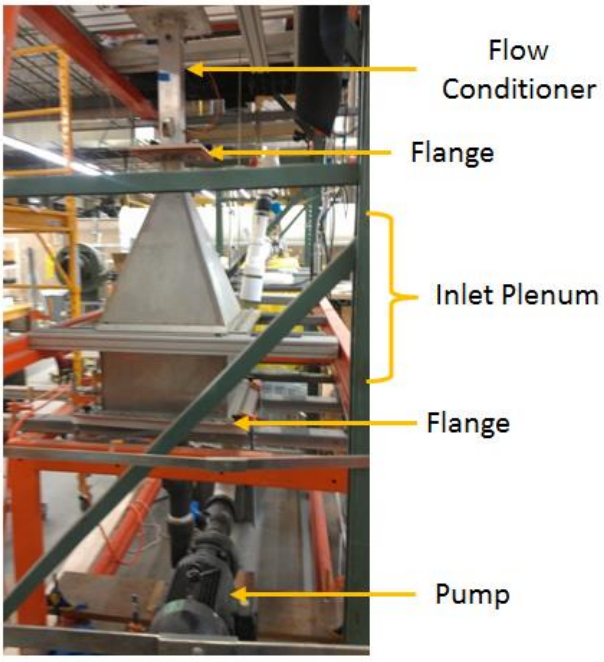

Figure 2: Inlet plenum of hydraulic loop.

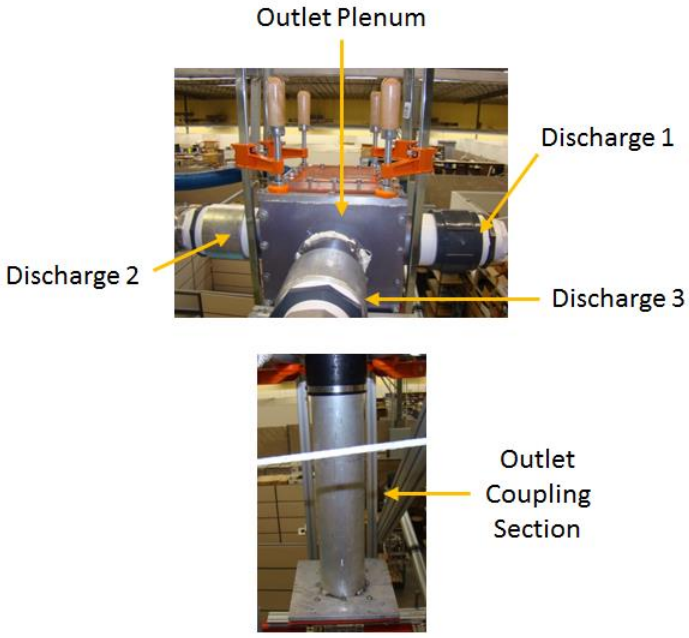

Figure 3: Outlet plenum of the hydraulic loop.

A flow diagram for the Texas A&M loop is provided in Figure 4. The loop is similar to the Clemson University test loop [19] where Westinghouse performed prior research. Unlike Clemson's horizontal loop, the Texas A&M loop is vertical allowing water to flow upward, which is consistent with actual fuel bundles. Another benefit to the Texas A&M facility is the ability to acquire data at much higher Reynolds Numbers than at Clemson. This capability is extremely important for future investigations and testing.

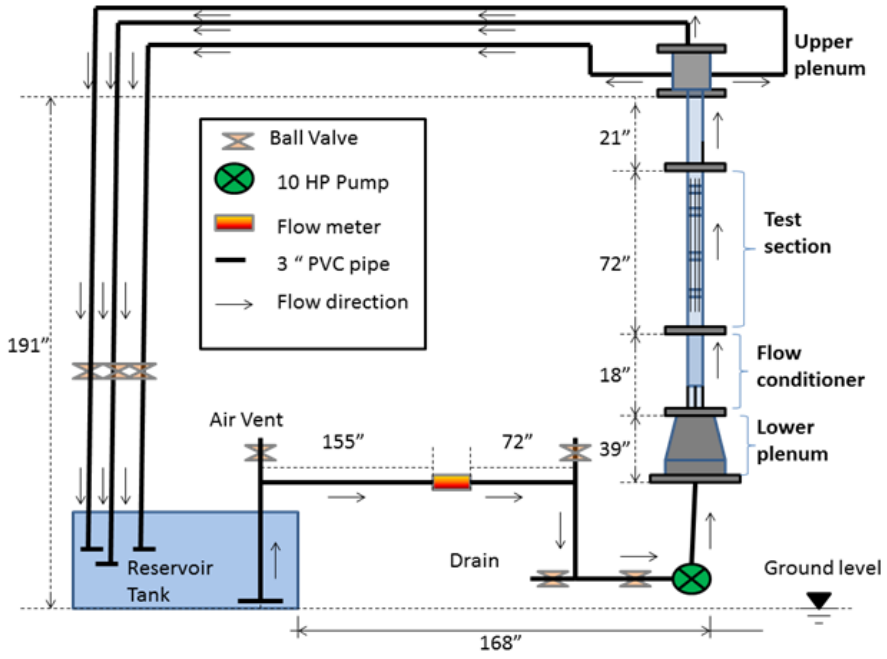

Figure 4: Flow diagram of the Texas A&M hydraulic loop.

2.2 General Test Assembly

The Texas A&M bundle is designed to allow for testing of 3 spans of representative bundle flow field conditions, thus requiring four grids in the flow field. Note that for testing, the top (most downstream) grid does not have to be of the same design as the testing grid since this grid is downstream of all measurements. A picture of the uninstalled bundle is provided in Figure 5. When the bundle is installed in the flow housing, the three vaned grids are held in axial position using 8 set screws per grid, accessible from the outside of the flow housing. The screws ensure that the grids do not shift under testing flow conditions and are used in place of bulging or specialized rods.

The test assembly is made up of the following:

- 3 Westinghouse V5H test grids (only inner straps tested), which are in the bundle flow region
- 1 support grid which is not in the bundle flow region
- 24 solid acrylic test rods (transparency required for certain laser tests)
- 1 instrumented rod (contains 2 miniature pressure transducers)

Solid acrylic rods were chosen for this test assembly due to their rigidity. Because there is a desire to obtain flow measurements using optical measurement techniques, a transparent material must be used in place of metal-clad rods. Additionally, since the ultimate goal is to achieve higher Reynolds Numbers in this test loop, it was necessary to choose a rod material that would retain some degree of rigidity to appropriately ascertain vibration effects due to fluid flow conditions. The previous rod type, fluid encased in plastic, proved too flexible at higher flow rates and disturbed flow characteristics such as subchannel vortices downstream of the mixing grid.

A detailed layout of the instrumented rod location is shown in Figure 6.

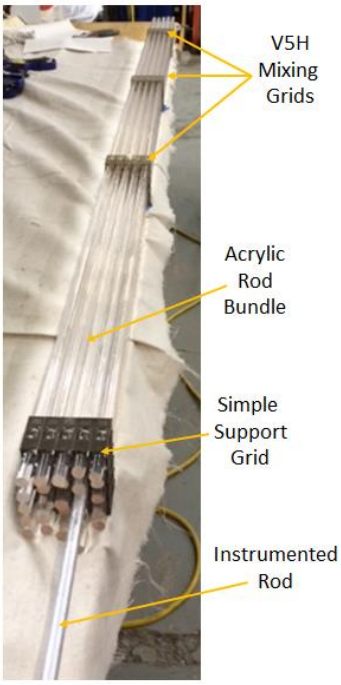

Figure 5: Test bundle before installation within test loop.

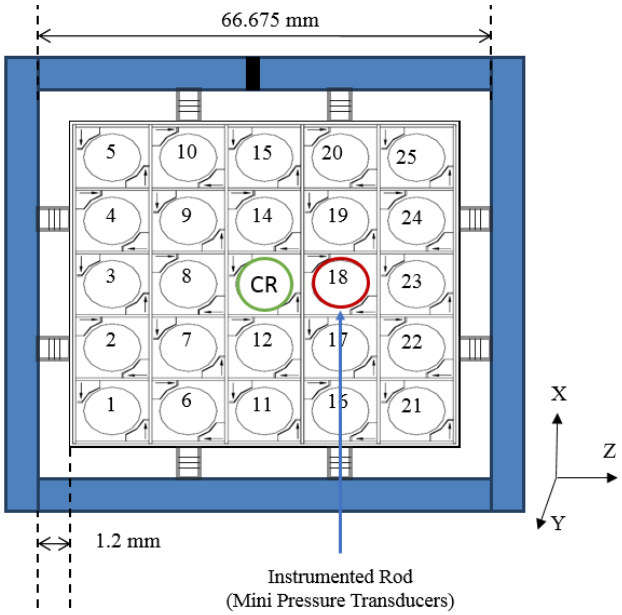

Figure 6: Rod bundle cross section designating location of instrumented rod.

2.3 Test Conditions

The primary controlled parameter during testing was bundle velocity. Two velocities were used: 2.48 m/sec and 3.66 m/sec. Table 1 provides a conversion from the gpm flow indicator on the loop to velocity for the two test configurations.

Table 1: Conversion from liters/min to loop velocity.

Bundle Velocity	TAMU Test Flow
m/sec	Liters/min
2.48	397.5
3.66	537.5

Testing was conducted beginning with the center of the down sensor positioned at the top of the grid strap and continued until the down sensor was 400 mm downstream of the grid strap (defined in Figure 7). The 400 mm axial position is the last achievable measurement point in the span for this test bundle. During bundle fabrication, it was difficult to maintain proper grid position and consequently the test span is slightly shorter than the prototypic length.

Additionally, the instrumented rod, containing the two pressure transducers, was rotated from 0 to 180 degrees in 45 degree increments (see Figure 8). This allows for pressure fluctuation mapping of two subchannels around the central rod.

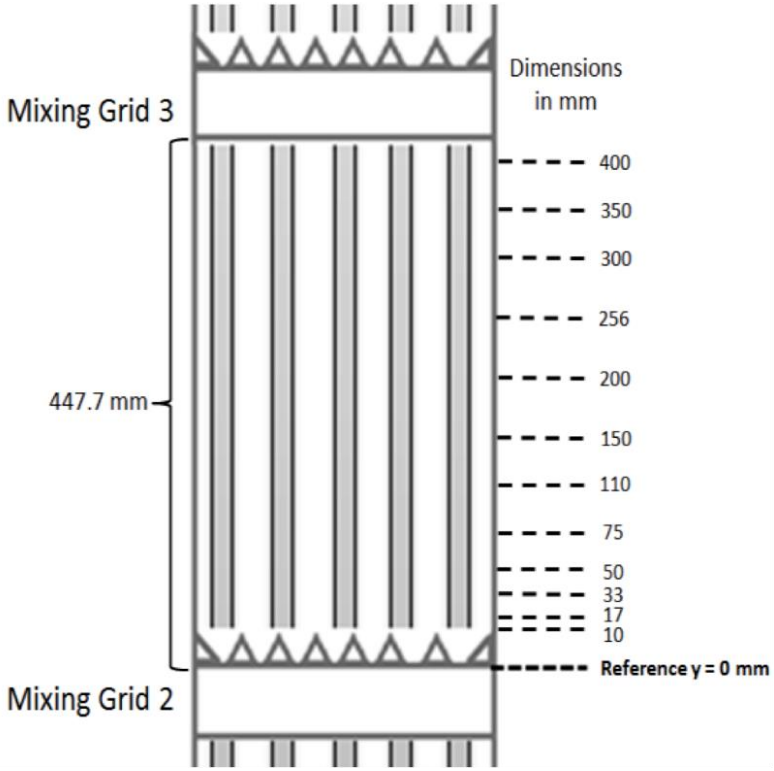

Figure 7: Experimental axial positions downstream of tested mixing grid.

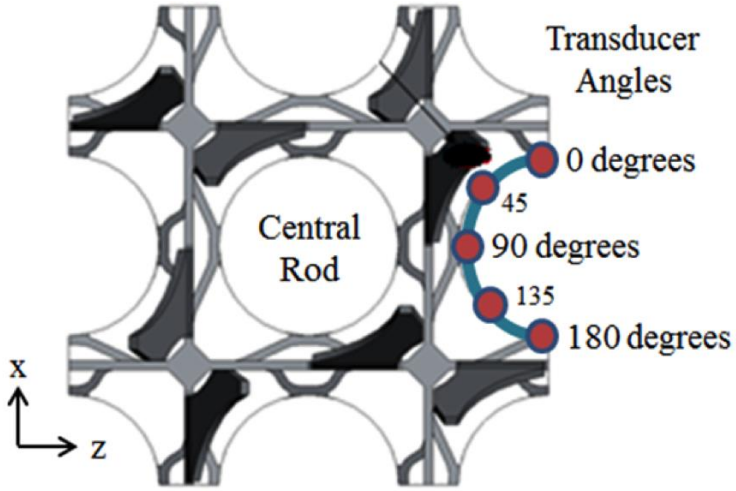

Figure 8: The five azimuthal positions at each experimental position.

2.4 Instrumentation and Calibration

Calibration of the miniature pressure transducers was performed before acquisition of test data. The two mini pressure transducers are fixed at a distance of 10 mm relative to each other using a custom-designed housing (see Figure 9). The custom housing and sensors are displayed in Figure 10 and a picture of the pressure transducers installed in the instrumented rod is given in Figure 11.

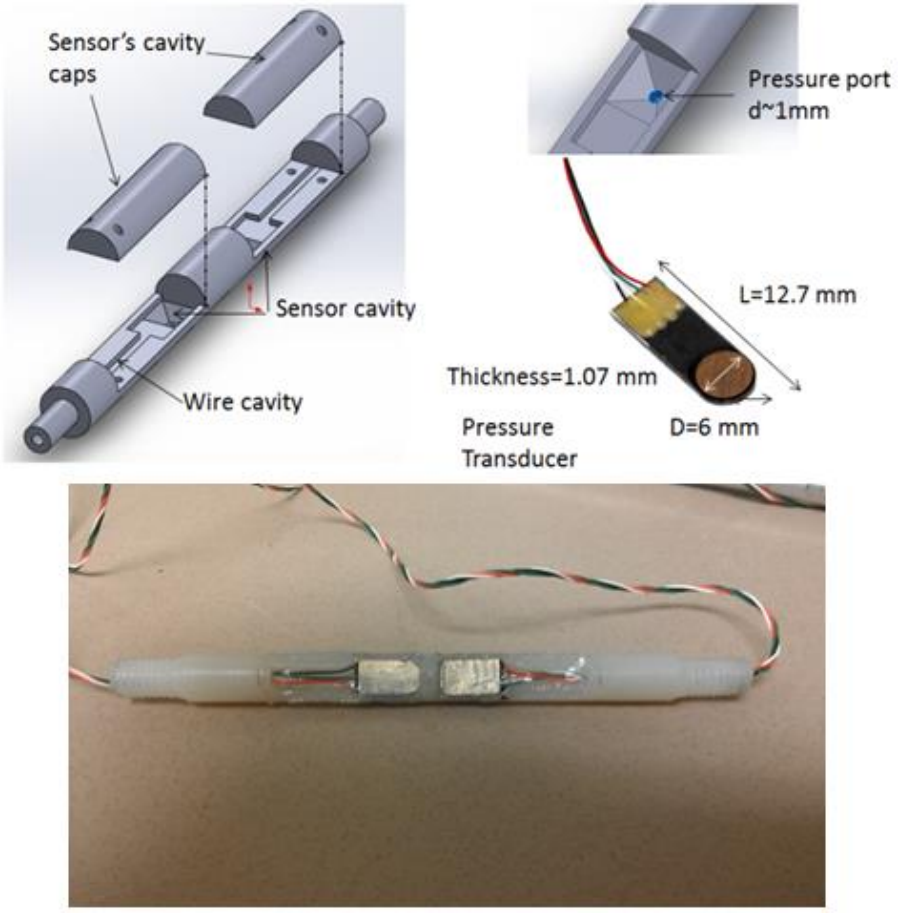

Figure 9: Picture and CAD drawing of the miniature transducers.

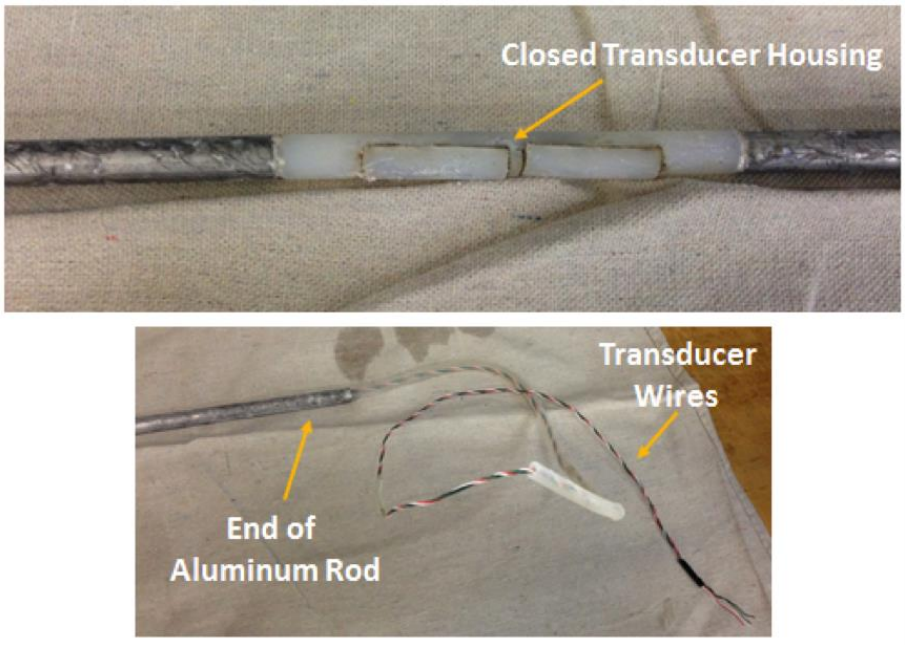

Figure 10: Picture of transducer housing installed in the aluminum rod.

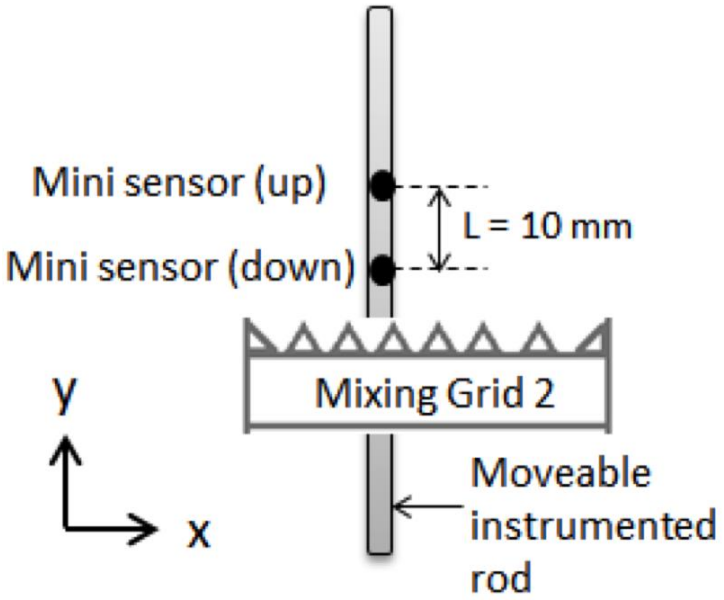

Figure 11: Sketch of installed instrumented rod and transducer relative position.

In February 2014, before the data was collected in May, the up sensor began to malfunction. The transducers were removed from their custom housing and the upper sensor repaired. Since repair work was performed on this sensor, and not by the manufacturer, the up sensor's effectiveness at providing accurate data is called into question. For this reason the analysis focuses on the down sensor.

2.5 Data Acquisition

Data was recorded through a National Instruments (NI) Data Acquisition module and the associated software. Each set of data was collected over a span of 10 seconds at a rate of 1 kHz. The collected data included:

1. Bundle Flow Rate (liters/min)
2. Axial Position (mm)
3. Azimuthal Position (degrees)
4. Instantaneous Voltage (V)

For each test velocity, data was collected at 13 axial positions (Figure 7) with 5 azimuthal positions (Figure 8) per each axial position. At each axial/azimuthal pairing, 3 data sets were acquired for statistical purposes. In total, 390 sets of data were collected.

3. DATA PRE-PROCESSING

The NI Data Acquisition module records instantaneous voltage from the pressure transducers. Since this is not the desired quantity, voltage must be converted to pressure through sensor-specific equations and is then used as the input for the data reduction and analysis process.

3.1 Data File Structure

The output from the NI software for each set of data is a directory. Each directory, an example is given in Figure 12, is named using the following convention:

Date_time_PMf*q*P*mm*degfs1ktest*

where f is the pump frequency, q is the flow rate, P is the axial and azimuthal position, fs1k is the sampling rate, test refers to one of three sets of data collected at each position, and * represents user input based on the testing conditions.

Within each of these directories are several files that are standard output from the NI software (defined in Figure 13). For this experiment, the “Custom_Voltage” and “mean” files resulted from data collection. The “Force” and “Inst” files are products of the MATLAB script discussed further in Section 3.2. Of the files listed in Figure 13, the one of interest for pre-processing is “Custom_Voltage.txt”. This text file, given in Figure 14, contains a header with information about the day and time of the acquisition as well as the time step, which is 0.001 seconds for all of the experimental IPM data sets. Below the header is the raw voltage data where each column represents a channel/sensor. There

are 8 columns in total, representing channels 0-7 or sensors 0-7. The channels of interest for this analysis are 4 and 5 since these correspond to the down and up transducers respectively. The rest of the channels are wall sensors, but channel 0 is neglected in the analysis because it is outside the test section. The "Custom_Voltage.txt" file from each directory is the instantaneous voltage input for the pre-processing Matlab script.

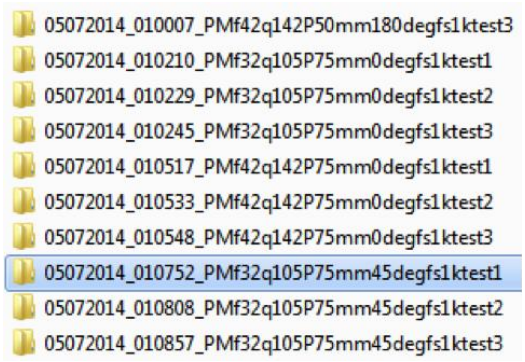

Figure 12: Example of directory naming convention.

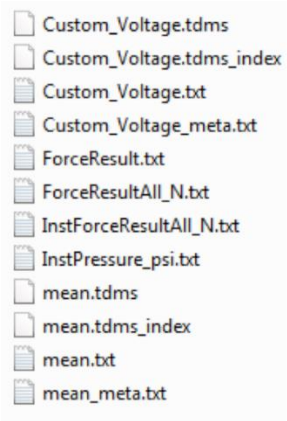

Figure 13: Example of directory contents where the InstPressure.txt contains the pre-processed IPM data.

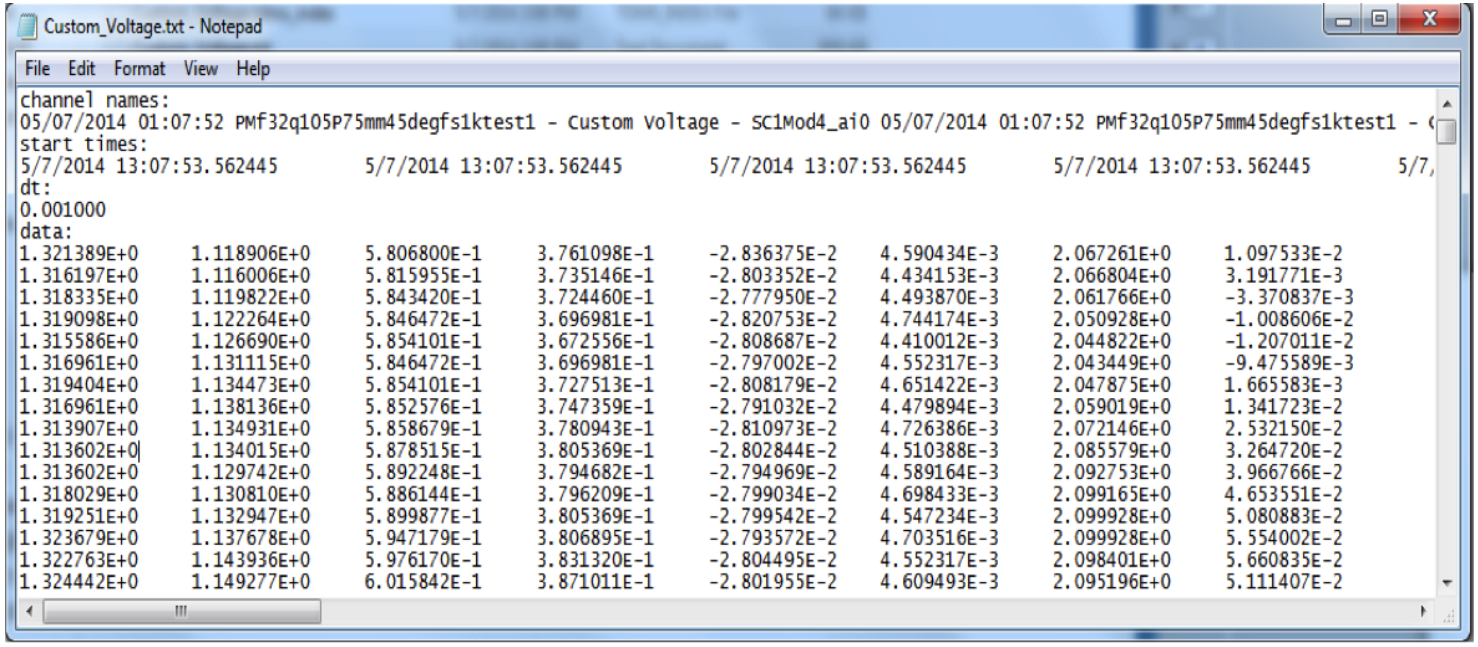

Figure 14: Example of Custom_Voltage.txt content which represents the raw data written from the data acquisition system.

3.2 The MATLAB Script

The purpose of the MATLAB script is to read in the raw voltage text files, strip the header to isolate the data, and convert the data to the desired form which is pressure in this case. Once the data has been converted from voltage to pressure, the script creates a new file in the same directory as the input file and writes the output instantaneous pressure to the new file.

3.2.1 Conversion of Voltage to Pressure

Voltage and pressure represent different physical phenomena but they can be linked. For the wall sensors, this relationship can be found in the reference documents from the manufacturer. The conversion equations for the transducers, on the other hand, were generated through calibration with one of the wall sensors. This means that for each azimuthal position, the two transducers required unique conversion equations, whereas the wall sensors did not. An example of the conversion equations for 0 degrees is given in Figure 15. The only changes that occur in Figure 15 from angle to angle are the equations for channels 4 and 5.

3.2.2 MATLAB Output

Once the data is converted to pressure, it is stored in a matrix that is then written to an output file in the same directory as the input file. For the purposes of the IPM analysis, these output files were named “InstPressure_psi.txt” (demonstrated in Figure 16). Each of these has a similar format to the raw voltage data found in “Custom_Voltage.txt” but without the multi-line header. “InstPressure_psi.txt” has a one-line header that describes which column corresponds to each sensor to aid in user

understanding. “InstPressure_psi.txt” is the file that is used as input for the data reduction and analysis process.

```
56        % 0 degrees
57 -      for i = 1:length(ch4)
58          % ch0 (0-30 psig)
59 -          psi0(i,:) = (6.0216*ch0(i,:)-0.0983);
60          % ch1 (0-15 psig)
61 -          psi1(i,:) = (3*ch1(i,:)-0.074);
62          % ch2 (0-5 psig)
63 -          psi2(i,:) = (1*ch2(i,:)+0.0013);
64          % ch3 (0-15 psig)
65 -          psi3(i,:) = (3*ch3(i,:)-0.074);
66          % ch4
67 -          psi4(i,:) = (130.47*ch4(i,:)+4.1838);
68          % ch5
69 -          psi5(i,:) = (189.44*ch5(i,:)-0.1729);
70          % ch6 (0-15 psig)
71 -          psi6(i,:) = (3*ch6(i,:)-0.074);
72          % ch7 (0-5 psig)
73 -          psi7(i,:) = (1*ch7(i,:)+0.0013);
74 -      end
```

Figure 15: Example of the voltage to conversion equations in the MATLAB script.

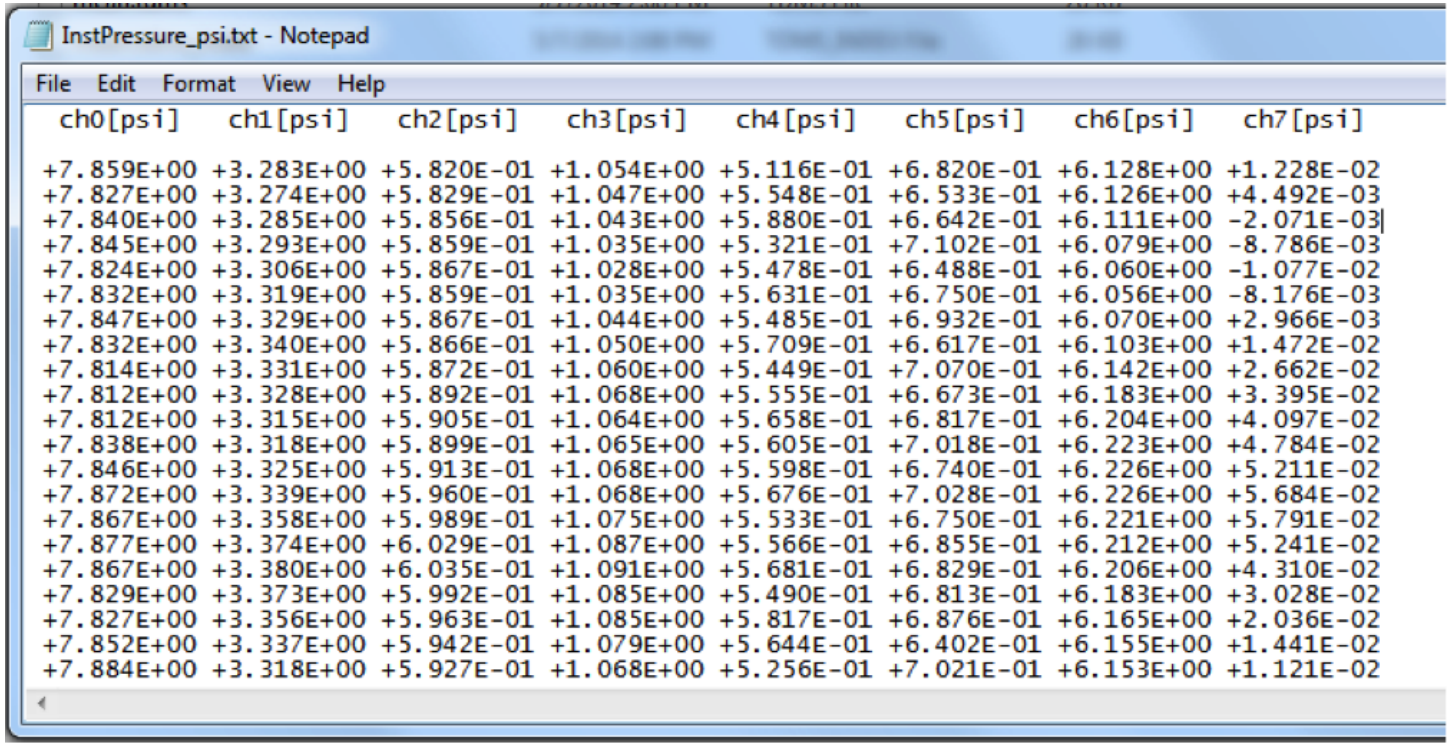

Figure 16: Example of the output of the voltage to pressure MATLAB script.

4. CFD METHODOLOGY

In conjunction with the experimental IPM data analysis, two CFD simulations (designated S1 and S2) were originally constructed in STAR-CCM+ v8.06.005 to serve as a validation tool for this measurement. Both models use the same geometry as the Texas A&M bundle and were based on the CFD model in Yan et al. [18]. While constructed in v8.06.005, both cases were run using the latest available version of STAR-CCM+, v9.04.009.

S1 originated as part of a summer internship at Westinghouse Electric Company and features a uniform velocity inlet condition. S2 has the same geometry, similar physics and mesh characteristics as S1 but features a non-uniform velocity inlet condition. The purpose of S2 is to evaluate the difference between defining a non-uniform velocity inlet condition and the conventional use of a uniform velocity condition. Specifics relating to the generation of the non-uniform velocity inlet condition are given in Section 4.1.3.

4.1 Computational Geometry and Boundary Conditions

4.1.1 Geometry

A 5 x 5 rod bundle geometry representative of a 17 x 17 design was used in both CFD analyses. This geometry features a rod diameter of 9.45 mm and rod bundle pitch of 12.6 mm, which are the same as a 17 x 17 square lattice fuel design. Contained within

this geometry is one mixing vane grid identical to the V5H design tested experimentally in the hydraulic loop.

The geometry presented in this study is the same that was used in the work by Yan et al. [18] in order to continue benchmarking hydraulic parameters obtained from the Texas A&M loop. The geometry was maintained to continue the study as part of a collaborative summer internship at Westinghouse Electric Company.

The axial domain of the 5 x 5 array is 254 mm in length, which represents half of a test section span. A schematic of the geometry is given in Figure 17. Due to time and computing constraints, the 254 mm length was maintained despite the availability of full span experimental data. The half span begins 50.8 mm upstream of the mixing grid lower weld nugget and ends 165.1 mm downstream of the upper weld nugget. The cross sectional dimensions of the 5 x 5 array are identical to the experimental test section, 66.675 mm by 66.675 mm. In this work, the streamwise direction is defined by the y-axis, while the x and z-axes define a cross section.

The set screws that were used in the experimental test section were not modeled in the numerical geometry. This may prove a possible source of error near the outer boundary of the array, but should not impact the results near the central rod, which are the focus of this study. The geometry is summarized in Table 2.

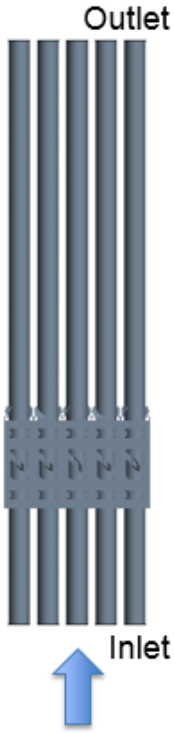

Figure 17: Geometry used for S1 and S2.

Table 2: Specifics of the S1 and S2 geometry.

Array Shape	Square
Array Size	5x5
Cross section	66.675 mm
Axial Domain	254 mm
Upstream Length	50.8 mm
Downstream Length	165.1 mm
Rod Diameter	9.45 mm
Bundle Pitch	12.6 mm
Hydraulic Diameter	11.78 mm
Streamwise Direction	Y-axis
Cross Section	X-axis and Z-axis
Grid Type	Westinghouse V5H
Grid Features	Dimples/Springs/Vanes

4.1.2 Boundary Conditions

A velocity inlet condition was assigned to the inflow of each simulation. A uniform inlet velocity of 2.48 m/s was used for S1. The inlet velocity specification for S2 was obtained from the outlet velocity profile of a periodic boundary simulation that was performed with only rods (see Section 4.1.3). The results of this analysis will determine if there is a difference in the results between simulations based on the inlet condition and if a uniform velocity condition will yield a similar result to experimental data.

In both simulations, the specified turbulence intensity is 1% and the turbulent length scale is 20% of the hydraulic diameter. These turbulence parameters were assumed by Yan et al. [18] and not measured in the experiment which could lead to some uncertainty in the sensitivity of the results. A pressure outlet was used for the outflow of both simulations. The outlet pressure was set to 0 gage pressure with the rest of the quantities extrapolated using outlet gradients.

The rest of the geometries, rods, grid, and outer boundary of the fluid domain were defined as no-slip wall boundaries. Wall boundaries were assigned to the sides of the fluid domain to simulate flow housing of the test section. The boundary conditions for S1 and S2 are summarized in Table 3.

S1 and S2 were initially run using Reynolds-Averaged Navier-Stokes (RANS) to provide an initial solution for the transient simulation which was performed using Large Eddy Simulation (LES). The physics models used for S1 and S2 are given in Table 4.

4.1.3 Generating the Non-Uniform Velocity Inlet Profile

The purpose of a second LES simulation, S2, was to investigate how the results would change if fully developed flow were established numerically to obtain a velocity profile instead of assuming a constant uniform velocity is present before the tested grid.

The model used to obtain the non-uniform inlet condition uses the same 5x5 rod bundle geometry as S1 and S2, but without the mixing grid (see Figure 18). The inlet and outlet conditions were defined the same as in S1, but with the addition of a periodic interface. The interface will allow the flow to recirculate and become more fully-developed. The periodic interface used in the rods only simulation was defined by specifying a fully developed interface mass flow rate of 6.608 kg/s to match the experiment. A summary of the boundary conditions is given in Table 5

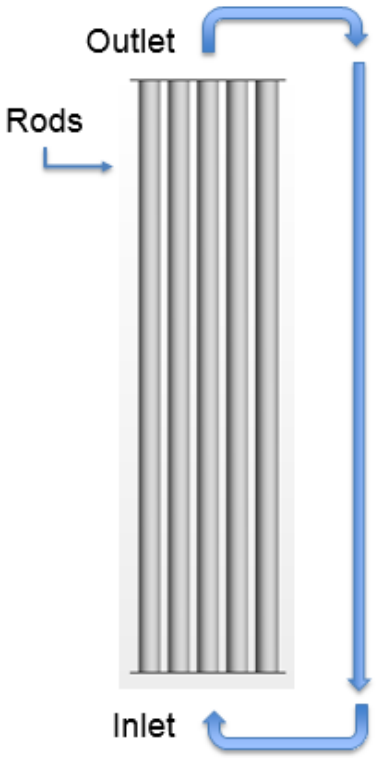

Figure 18: Schematic demonstrating the flow pattern used to obtain the inlet velocity boundary condition for S2. After convergence was reached, the outlet of this simulation was used as the inlet for S2.

Table 3: Boundary conditions for S1 and S2 respectively.

	Boundary	Condition	Definition
S1	Rods and Grid	Adiabatic wall condition	
	Inlet	Uniform constant velocity inlet	2.48 m/s
	Outlet	Constant pressure outlet	0 Pa
	Fluid domain boundary	Adiabatic wall condition	
S2	Rods and Grid	Adiabatic wall condition	
	Inlet	Non-uniform constant velocity inlet	2.46 m/s (Mean)
	Outlet	Constant pressure outlet	0 Pa
	Fluid domain boundary	Adiabatic wall condition	

Table 4: Physics models used during S1 and S2 runs.

	Physics Models	Details
Steady State	RANS	N/A
	K-Epsilon Turbulence	N/A
	Realizable K-Epsilon Two-Layer	2nd Order Wolfstein
	Constant Density	Room Temperature
	Segregated Flow	2nd Order
	Two-Layer All y+ Wall Treatment	N/A
	Linear Pressure Strain	2nd Order
	Gradients	Hybrid Gauss-LSQ
	Steady	N/A
	Turbulent	
	Three Dimensional	
	Liquid	997.561 kg/m^3
Initial Condition	Turbulence Intensity	0.01
	Physics Models	Details
LES	Large Eddy Simulation	N/A
	WALE Subgrid Scale	N/A
	Constant Density	Room Temperature
	Segregated Flow	Bounded Differencing
	All y+ Wall Treatment	N/A
	Gradients	Hybrid Gauss-LSQ
	Implicitly Unsteady	N/A
	Turbulent	
	Three Dimensional	
	Liquid	997.561 kg/m^3

Table 5: Rods only simulation boundary conditions.

Boundary	Condition	Definition
Rods	Adiabatic wall condition	
Inlet	Uniform constant velocity inlet	2.48 m/s
Outlet	Constant pressure outlet	0 Pa
Inlet & Outlet	Periodic Interface-Mass Flow Rate	6.608 kg/s
Fluid domain outer boundary	Adiabatic wall condition	

A steady-state run was performed using the Reynolds Stress Turbulence (RST) model, in addition to RANS (see Table 6). The mesh for the rods only case is a finer mesh than S1 or S2 with the same settings as the fine mesh in Section 4.2.1. The RST model was used because it solves 7 equations. Solution convergence using the RST model and a fine mesh ensures that fully-developed flow has been achieved.

4.2 Mesh Generation

Simulation S1 was meshed using STAR-CCM+ v6.06.017 as part of the previous analysis by Yan et al. [18]. The mesh was generated using the trimmer mesher with 2 prism layers at the wall boundaries to obtain boundary layers. A base size of 0.21 mm was defined for the S1 mesh resulting in a final mesh of approximately 76 million cells. The base size was determined based on the experience of Yan et al. [18]. A summary of the settings used to create the S1 mesh are provided in Table 7.

Table 6: Rods only physics models.

	Physics Models	Details
Steady State	Reynolds Stress Turbulence	N/A
	RANS	N/A
	Realizable K-Epsilon Two-Layer	2nd Order Wolfstein
	Constant Density	Room Temperature
	Segregated Flow	2nd Order
	High y+ Wall Treatment	N/A
	Linear Pressure Strain	2nd Order
Initial Conditions	Turbulence Intensity	0.01

Table 7: S1 mesh settings.

	Mesh Settings	Definition
Mesh Models	Prism Layer Mesher	
	Surface Remesher	
	Trimmer	
Reference Values	Mesh Base size	0.21 mm
	Maximum cell size	0.21mm
	Number of prism layers	2
	Prism layer stretching	1
	Prism layer thickness	0.42 mm
Number of Cells	76,680,347	

Since the use of only 2 prism layers slightly limits the definition of the boundary layers around the rods, a slightly different mesh was used for simulation S2. The S2 mesh was generated using STAR-CCM+ v.9.04.004 using the trimmer mesher. The same base size, 0.21 mm, was used to keep the simulation size manageable and to allow for some comparison between the two simulations. The S2 mesh features 4 prism layers which leads to a final mesh size of approximately 91 million cells. A summary of the mesh characteristics is given in Table 8. A side-by-side comparison of the two meshes is given in Figure 19.

Table 8: S2 mesh settings.

	Mesh Settings	Definition
Mesh Models	Prism Layer Mesher	
	Surface Remesher	
	Trimmer	
Reference Values	Mesh Base size	0.21 mm
	Maximum cell size	0.21mm
	Number of prism layers	4
	Prism layer stretching	1.2
	Prism layer thickness	0.42 mm
Number of Cells	91,656,239	

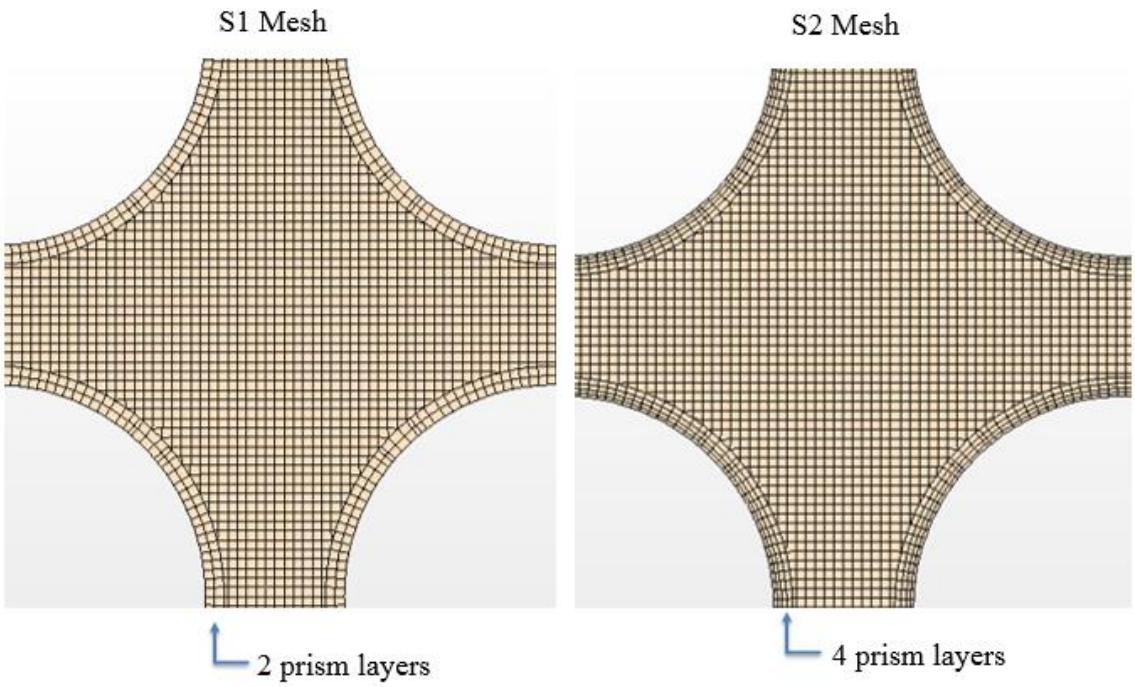

Figure 19: Side-by-side comparison of the two meshes utilized in this analysis.

4.2.1 Mesh Sensitivity Study

While Yan et al. was confident in the S1 mesh based on experience, but it was important for the completeness of the work that a mesh sensitivity study was performed for the S2 mesh. The following mesh sensitivity analysis was conducted using the Richardson Extrapolation approach outlined in Roach [20].

The sensitivity study was performed using three different cell base sizes. The medium size was fixed at the same base value as S1, 0.21 mm, to allow comparison between simulations later. The coarse and fine mesh base size were determined by

adding and subtracting 25% of the medium base size respectively. The settings for all three meshes are provided in Table 9.

Following the prescribed method, the grid convergence study was performed for the 17 mm/45 degrees position. The benefit to utilizing this position for this study is that turbulence in this region of the tested geometry is very high. Proving grid convergence at this position, where the flow is more likely to vary between meshes due to resolution, will give insight into the convergence of the entire mesh.

As part of the Richardson extrapolation, the pressure at zero grid spacing must be determined based on the relationship between the two finest grids (the fine and medium meshes in this study). This point represents the true value that cannot be achieved, but with finer and finer mesh base sizes, it is possible to get closer to the ideal value.

Table 9: Settings used to conduct mesh sensitivity study.

	Mesh Settings	Definition
Mesh Models	Prism Layer Mesher	
	Surface Remesher	
	Trimmer	
Reference Values		
General Characteristics	Number of prism layers	4
	Maximum cell size	100% of base
	Prism layer stretching	1.2
	Prism Layer Thickness	200% of base
Coarse Mesh	Mesh Base size	0.2625 mm
	Number of Cells	50,156,621
Medium Mesh	Mesh Base size	0.21 mm
	Number of Cells	91,656,239
Fine Mesh	Mesh Base size	0.1575 mm
	Number of Cells	204,960,727

The results of the grid convergence study for 17 mm/45 degrees are given in Figure 20. The orange point at 0 normalized grid spacing is the Richardson extrapolation point, while the points in blue represent the pressure results in increasing grid base size from fine to coarse. The estimated value of the instantaneous pressure fluctuation at this position is 0.20 psi +/- 2.02%. The 3 grid solutions were checked to determine if they were in the asymptotic range of convergence by computing two Grid Convergence Index values over 3 grids. This calculation yielded a value of 1.08 which is approximately 1, meaning the solutions from all 3 grids are well within the asymptotic range of convergence.

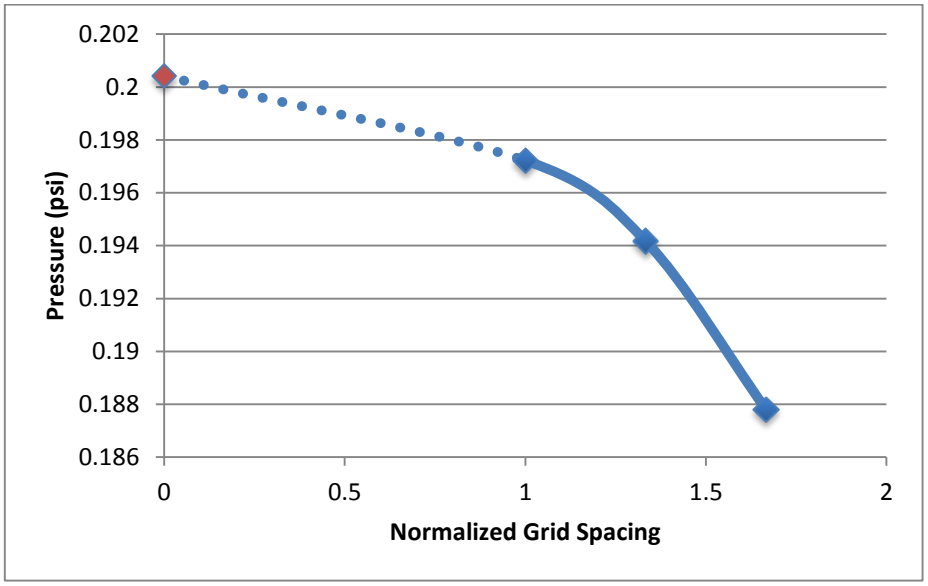

Figure 20: Grid convergence using the 17 mm/45 degree position.

4.3 Solution Method

For simulations S1 and S2 a steady state analysis was performed and used as the initial guess for the transient analysis. Each analysis was performed under the same conditions as the experimental data: atmospheric pressure with an adiabatic room temperature condition.

4.3.1 Steady State Analysis

The steady state analysis was performed using RANS with the quadratic version of the κ-ε turbulence model [18]. Simulations S1 and S2 were run until convergence was confidently reached. Convergence occurred at approximately 1,500 iterations for S1 and 1,000 iterations for S2.

The steady state solution for S1 was used as the starting solution for the transient simulation. The same process was used for S2 with the exception that the inlet condition was changed from a uniform velocity inlet to a non-uniform velocity inlet.

4.3.2 Transient Analysis

An unsteady LES with the WALE (Wall-Adapting Local-Eddy viscosity) model was chosen to simulate sub-grid scale turbulence in this application. The use of LES with the WALE model was validated in the previous work by Yan et al. [18].

The time steps of S1 and S2 were initially different, with the time step of S1 defined at 1e-5 seconds and the S2 time step at 1e-4 seconds. Due to time constraints, both simulations were run using a time step of 1e-4 seconds upon reaching transient steady state at 2.4 seconds of physical time (4 times the vortex shedding time). The convective Courant number was calculated for each simulation based on the mean inlet

flow velocity, the time step, and the characteristic mesh size. The Courant number of S1 at 1e-5 seconds is 0.118 and 1.18 at 1e-4 seconds. While the final Courant number is above 1, it is not significantly high and was necessary due to simulation run time constraints. The mean inlet flow velocity of simulation S2 is 2.46 m/s which results in a Courant number of 1.17 at 1e-4 seconds. Again, while this is slightly high, the length of time it took to reach 2.4 seconds became a crucial factor when deciding on which time step to use.

In S1 and S2, the RANS solution was used as the initial condition for the LES analysis. Both simulations were run to 2.4 seconds to reach transient steady state and then continued to collect data for 1 full second of physical time under transient steady state conditions. The data collected during this time period will provide a more equitable comparison to experimental data.

4.3.3 CFD Data Acquisition

Upon reaching 2.4 seconds of physical time for both simulations, pressure and velocity data was exported to .csv files. The exported data and corresponding sampling rate are as follows:

1. Pressure and Velocity Plane Data – Sampling rate: 1 kHz (0.001 seconds)
    a. Absolute Pressure
    b. Tangential Velocity
    c. Velocity [i, j, k]
    d. Velocity Magnitude
    e. Cell Locations [x, y, z]

2. Pressure Probe Data – Sampling rate: 10 kHz (0.0001 seconds)
3. Other Plane Data – Sampling rate: 0.1 kHz (0.01 seconds)
    a. Helicity
    b. Convective Courant Number
    c. Turbulent Viscosity
    d. Vorticity Magnitude
    e. Vorticity [i, j, k]
    f. Cell Locations [x, y, z]

The cross-sectional plane data (above list items 1 and 3) were collected at 1 hydraulic diameter upstream of the grid, as well as 10, 17, 33, 50, 75, 110, and 150 mm downstream of the top of the grid strap. The point probe data was collected at the same 5 azimuthal positions and half the axial positions (up to 150 mm) of the experimental positions. The lateral planes and a side view of the pressure probes are provided in Figure 21. Figure 22 gives the top down view of the probe locations. It should be noted that the coordinate system used to define the simulation differs from the experimental coordinate system. This discrepancy was addressed in this analysis to insure data comparison at the proper orientation.

All pressure and velocity data was collected at a minimum sampling rate of 1 kHz to provide adequate resolution and to compare with the experimental data sampled at 1 kHz.

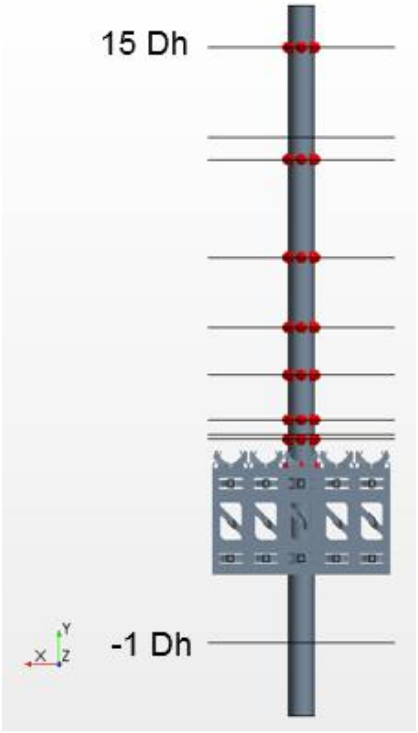

Figure 21: Lateral view of the axial domain illustrating the relative locations of the lateral planes and point probes.

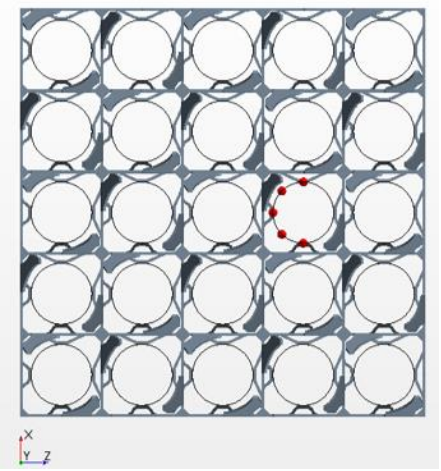

Figure 22: Top down view illustrating pressure probe relative locations. Note that the simulation coordinate system is different from the experimental coordinate system and has been addressed throughout this analysis.

5. COMPARISON OF PRESSURE PROBE DATA

Two types of analyses were performed using the pressure probe data collected by simulations S1, S2, and the experimental data. The first analysis dealt with each individual azimuthal position while the second analysis was to compare like angular positions and dissimilar angular positions. The goal of these analyses is validate the results of the experimental pressure transducers with CFD point probes at the same azimuthal and axial positions.

To compare both CFD simulation results to the experimental instantaneous pressure measurements, all data was normalized by the mean axial pressure value (pressure averaged over each axial point) for each case respectively. The following plots contain normalized pressure at a physical time of 3.5 seconds, which was chosen because it is significantly after simulation has reached steady state transience.

5.1 Individual Azimuthal Positions

The normalized instantaneous pressure measurements are displayed two ways in the following sub-sections: comparison of the two CFD simulations and a comparison between the CFD results and Experimental data. The purpose of showing the CFD results in a separate figure is to more easily discern the data trends.

5.1.1 0 Degrees

The instantaneous pressure from the CFD simulations at each 0 degree position is given in Figure 23. The 0 degrees position represents the instantaneous pressure seen by

the rod surface in a rod gap. The axial positions are normalized using the hydraulic diameter of a subchannel (see Table 2).

Both simulations result in same trend with a minimal difference in values. This means that both simulations are predicting approximately the same values. As previously mentioned, the next step is was to compare the CFD results with the corresponding experimental results (see Figure 24).

As evident in Figure 24, the CFD results represent the average pressure fluctuations in the experimental data at the 0 degree azimuthal position. Additionally, the CFD results are approximately constant when plotted on the same scale as the experimental data. The maximum percent difference is 20% at 0 y/Dh and the minimum percent difference is 0% at 3 y/Dh.

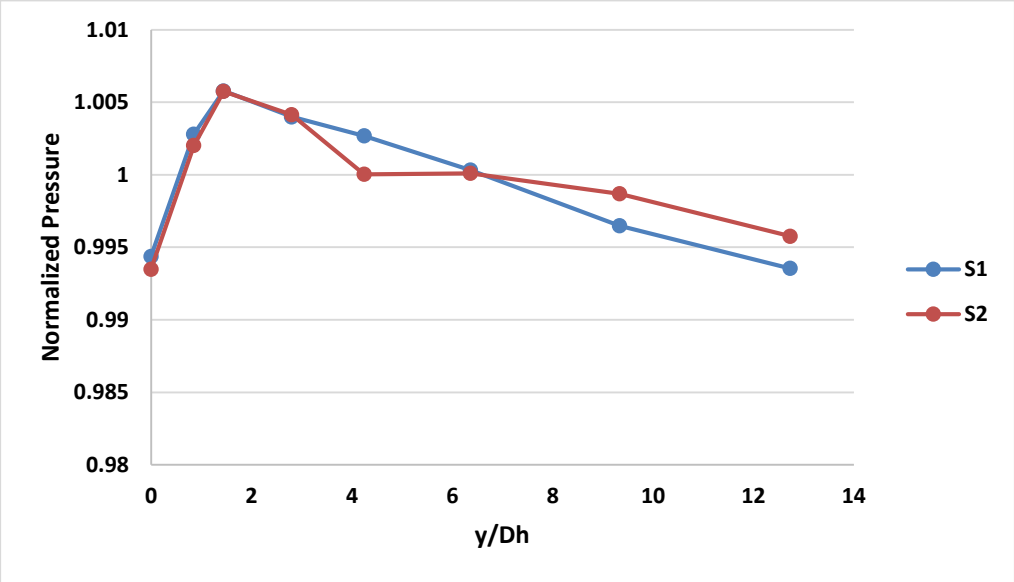

Figure 23: Normalized pressure at 0 degrees from S1 and S2.

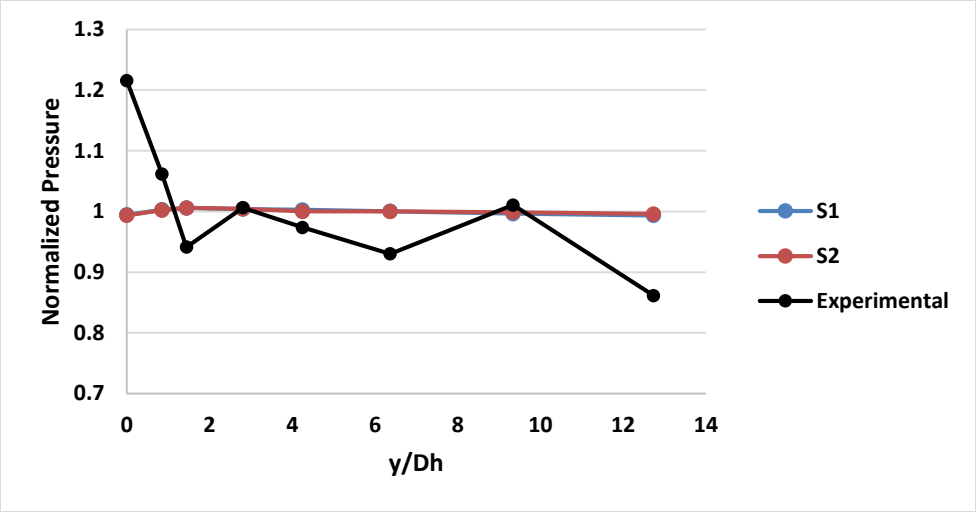

Figure 24: Comparison of S1, S2, and the experimental data at 0 degrees.

5.1.2 45 Degrees

The same analysis was performed for the positions at 45 degrees. The difference between this position and 0 degrees is that the probe is pointed into the center of the subchannel instead of a rod gap. The CFD results are given in Figure 25. As with the 0 degree position, the two CFD results are highly similar with very little variation between the two simulations and between 0 and 13 y/Dh. Unlike the 0 degree position, however, the 45 degree trend is not an initial peak that dies at greater y/Dh, it is decreasing in a more linear fashion. A plot of all three data sets at 45 degrees is presented in Figure 26.

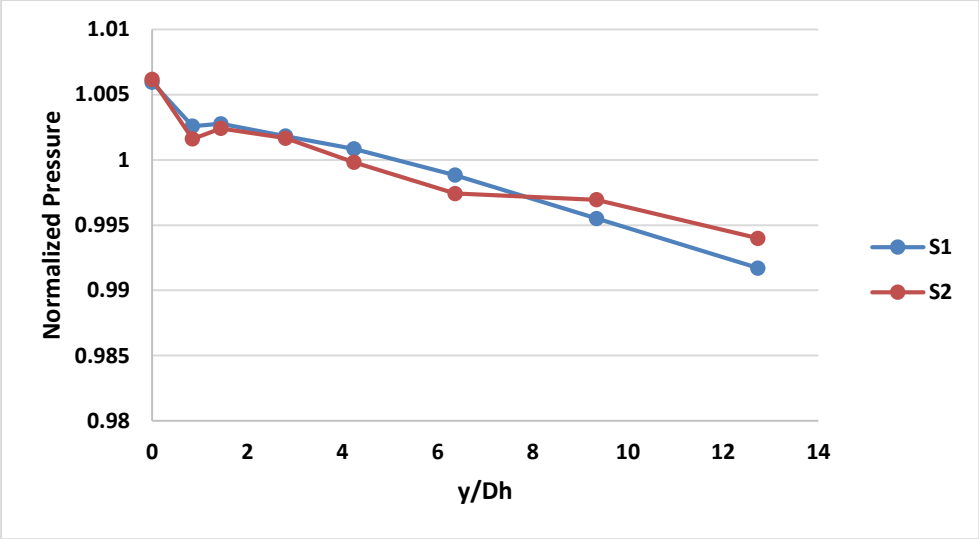

Figure 25: Normalized pressure from S1 and S2 at 45 degrees.

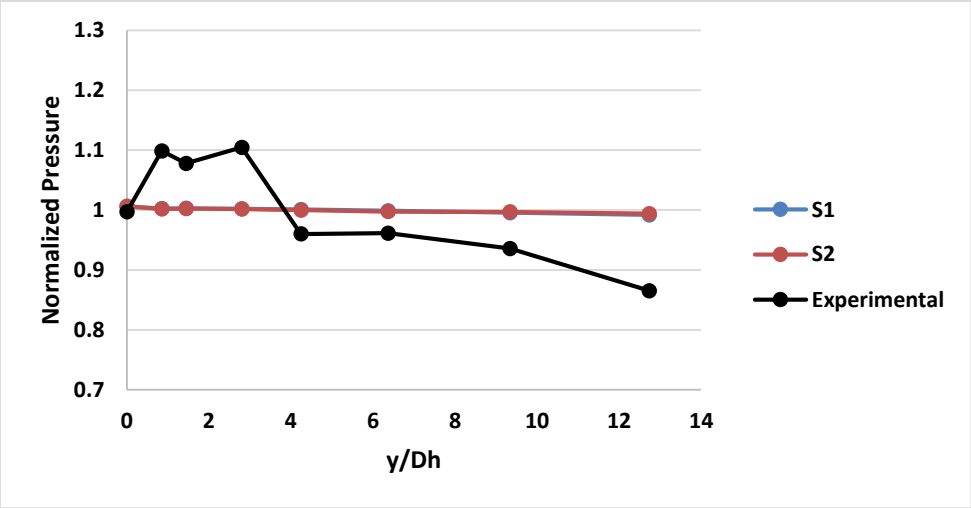

Figure 26: Comparison of S1, S2, and experimental data at 45 degrees.

CFD and experimental data is comparable at 45 degrees. Despite the appearance of nearly constant instantaneous pressure, the CFD results fall within the median of the

experimental data values for pressure. It is also important to note that the experimental data trend for 45 degrees is completely different than at 0 degrees, with a more pronounced peak at lower y/Dh. The maximum percent difference for this comparison is 13.8% at approximately 13 y/Dh. The minimum percent difference remains 0 at 0 y/Dh.

5.1.3 90 Degrees

The 90 degree position is another position that points into a rod gap, therefore making it geometrically similar to the 0 degree position. Figure 27 shows the results from simulations S1 and S2. Unlike the other positions thus far, the 90 degree position experiences the most variation in the instantaneous pressure shape of both simulations. S1 experiences a minor peak around 1 y/Dh whereas S2 peaks downward at 1 y/Dh, upward at approximately 2 y/Dh, and downward at 3 y/Dh, before settling and following S2 from approximately 4 to 13 y/Dh.

The trend of data in Figure 27 does appear similar to the peaked trend in Figure 18, however. This corresponds with the similar geometry seen by the 0 and 90 degree probes. The experimental results at 90 degrees were then added in Figure 28.

Interestingly, the trend at 90 degrees closely resembles the trend at 45 degrees shown in Figure 26. A peak exists in the experimental data from 0 to 4 y/Dh before slowly decaying. The main shape variation between 45 and 90 degrees is that the experimental data at 90 degrees appears asymptotic between 11 to 13 y/Dh whereas the slope in experimental data over the same range at 45 degrees is much larger. Again, the CFD data is approximately constant and exists in the middle of the experimental range.

The maximum percent difference is 12.5% at approximately 13 y/Dh and the minimum percent difference is 0% at 4 y/Dh.

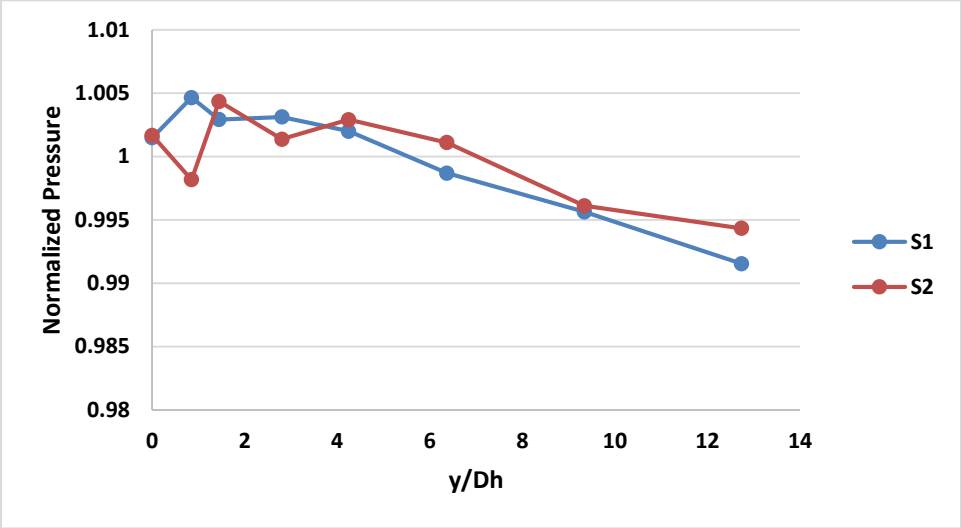

Figure 27: Normalized pressure from S1 and S2 at 90 degrees.

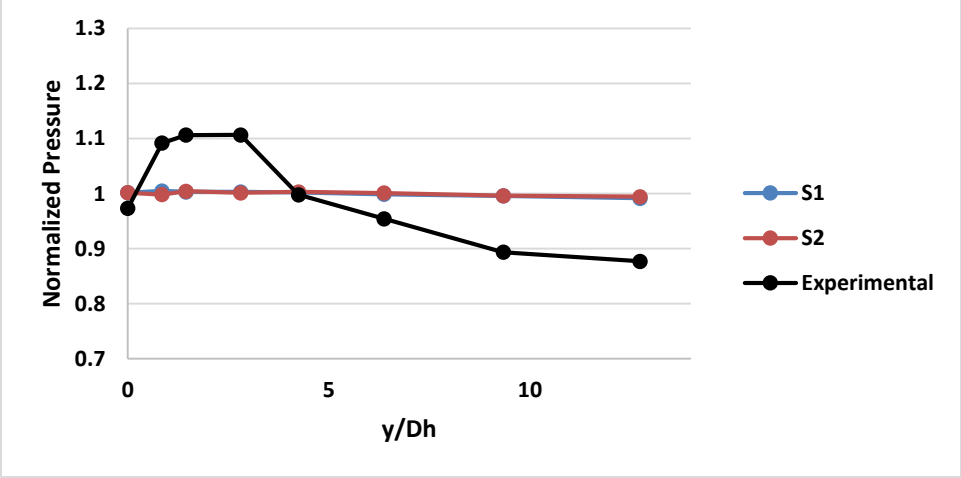

Figure 28: Comparison of S1, S2, and experimental pressure data at 90 degrees.

5.1.4 135 Degrees

Similarly to the 45 degree position, 135 degrees points into the center of a subchannel. The CFD results at 135 degrees are provided in Figure 29. Since 135 degrees points into the subchannel like the 45 degree position, the expectation is that the results at these two positions would be similar in trend. This is not the case, however, because 135 degrees exhibits two peaks before decreasing. Also, unlike 45 degrees, the pressure at 0 y/Dh is one of the lowest points for the 135 degree data instead of the highest. A plot of the CFD with the 135 degree experimental data is given in Figure 30.

Despite the variation in Figure 29, Figure 30 appears similar in shape to the 45 degree position. The amplitude of the peak is slightly less than the 45 degree position, but occurs over the same y/Dh range. Additionally, a similar downward slope exists from 11 to 13 y/Dh. The maximum percent difference for 135 degrees is 13.4% at approximately 13 y/Dh and the minimum, 0%, occurs at 0 y/Dh. The positions of the maximum and minimum percent differences are the same for the 45 and 135 degree positions.

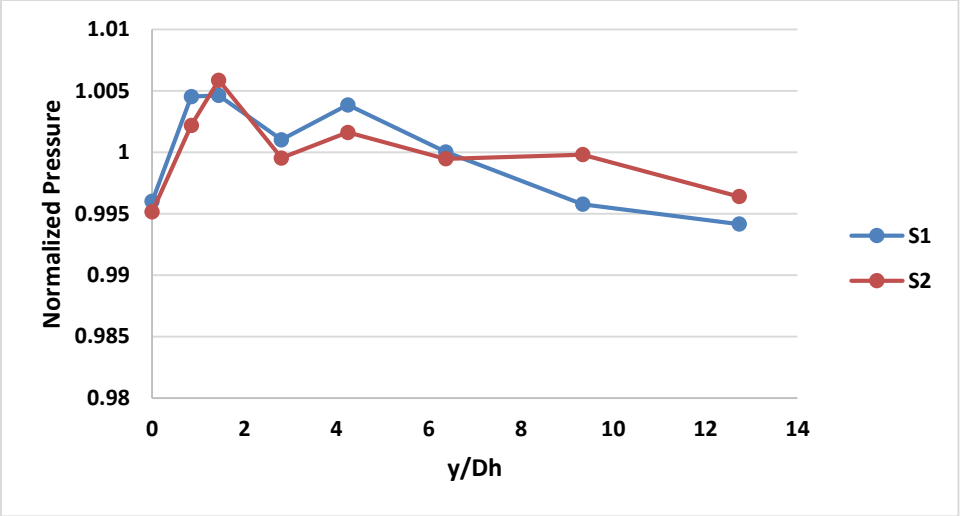

Figure 29: Normalized pressure of S1 and S2 at 135 degrees.

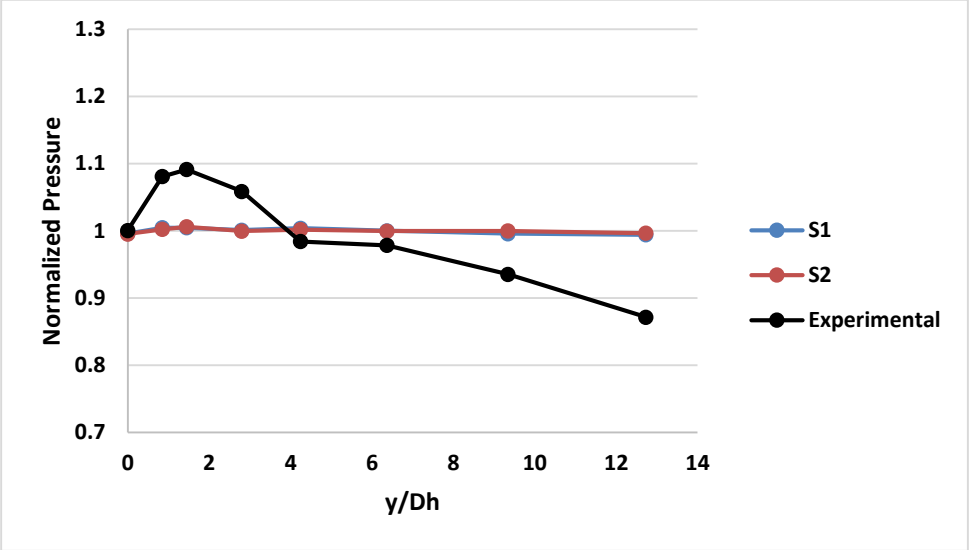

Figure 30: Comparison of S1, S2, and experimental data at 135 degrees.

5.1.5 180 Degrees

The last azimuthal position, 180 degrees, points into a rod gap similar to the 0 and 90 degree positions. The CFD normalized pressure results are given in Figure 31. The shape of the data for both simulations at 180 degrees closely resembles the trends at 0 degrees (see Figure 23). Pressure peaks around 2 y/Dh and then slopes downward almost linearly.

When compared to 90 degrees, the other rod gap position, there is more variation. The 90 degree position experiences the same decreasing trend from approximately 2 y/Dh, but does not exhibit the initial peak as prominently as the 0 and 180 degree positions. To fully compare the 0, 90, and 180 degree positions, the experimental data was added in Figure 32. The normalized pressure trend at 180 degrees loosely resembles the 90 degree position. There is a peak, but not as broad as the 90 degree position. Additionally, a similar asymptotic trend exists at approximately 13 y/Dh as at 90 degrees.

Conversely, the results at 180 degrees do not resemble the 0 degree data nor did the 90 degree position. In fact, at every position other than 0 degrees, peaks are present in the lower range of y/Dh and the CFD results represent the median of the experimental profile.

For the 180 degree position, the maximum percent difference is 11.8%, occurring at approximately 1.5 y/Dh, and the minimum of 0% difference occurs at 4.2 y/Dh. To better display the similarities between the simulation and experimental results, Figure 32 was plotted again with two axis and provide in Figure 33. When plotted in this manner it

is easy to see that the CFD results have the same general trend as the experimental data except that CFD over estimates the pressure close to the grid and underestimates the pressure past 6 hydraulic diameters. This confirms that the simulations are predicting the rise in pressure near the grid and the decrease downstream and with additional research the difference in results might lessen. Another interesting point to make is that the CFD probes calculate pressure based on the area of the cell containing the probe. Some of the difference between the simulated and measured values could be because pressure is being calculated over a smaller area than the experimental pressure transducer.

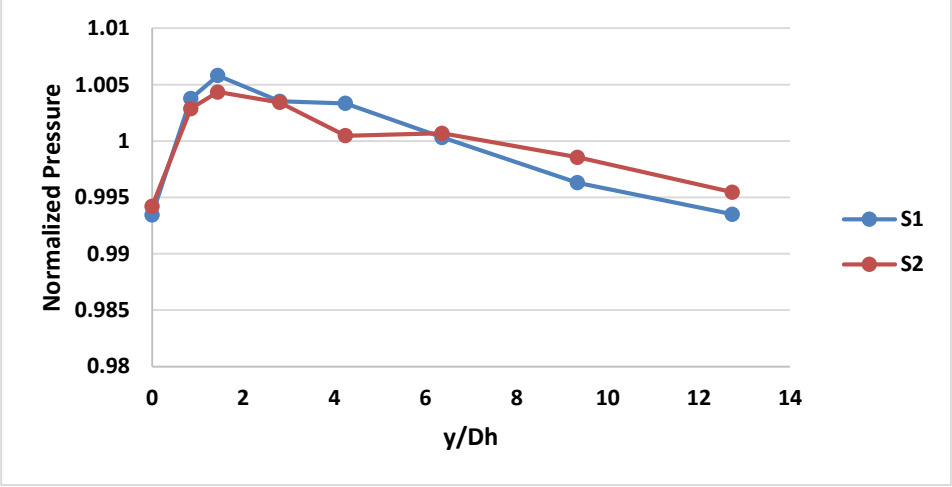

Figure 31: Normalized pressure from S1 and S2 at 180 degrees.

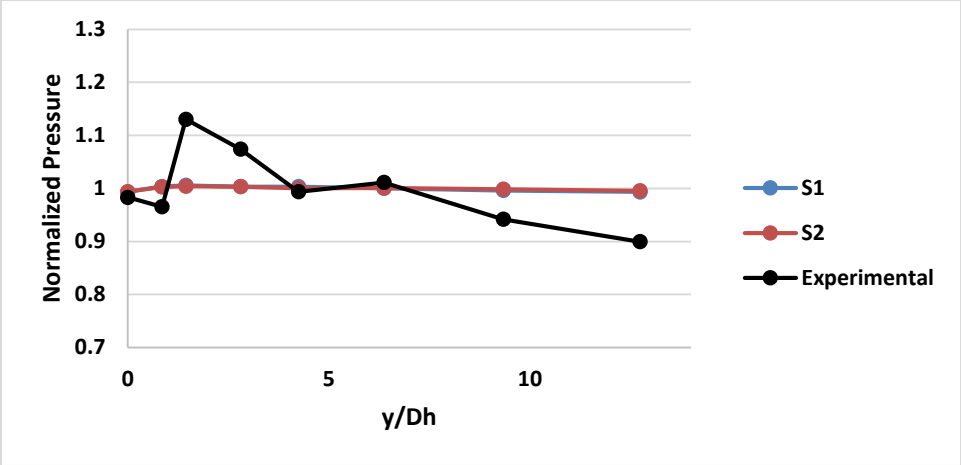

Figure 32: Comparison of S1, S2, and experimental data at 180 degrees.

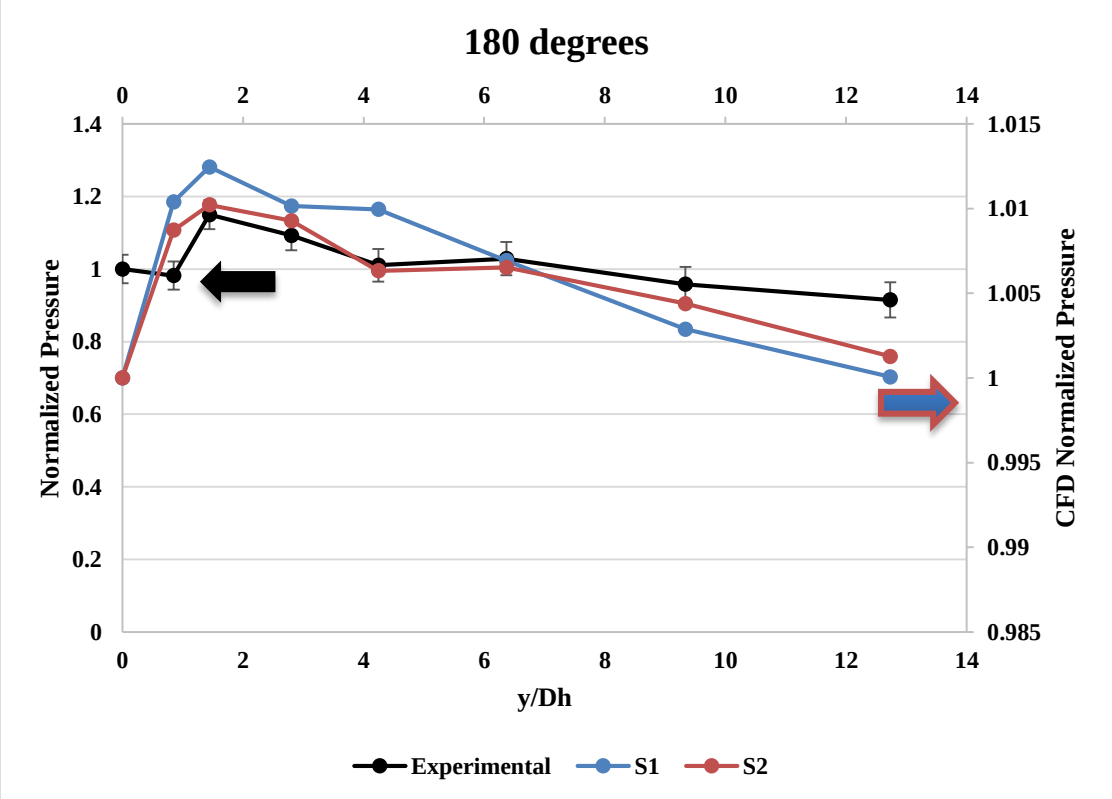

Figure 33: Comparison of S1, S2, and experimental data with two axes.

5.1.6 Individual Azimuthal Position Summary

Overall, a consistent pattern was not discovered in this analysis. While the CFD results for 0 degrees and 180 degrees appear similar, the experimental data for the same two positions is not similar in trend. There were similarities in shape of the experimental data at 45, 90, 135, and 180 degrees, but no significant distinction between rod gap and subchannel results except in the range of 11 to 13 y/Dh. In this range, the 45 and 135 degree positions experience downward sloped pressure whereas the 90 and 180 degree positions become approximately asymptotic between 11 and 13 y/Dh. The outlier for the experimental data is the 0 degree position and the outlier for CFD appears to be the 45 degree position.

Instantaneous pressures obtained from the two CFD simulations agreed with the experimental data within 10%, however, simulations under-predicted pressures compared to experimental data. Further testing and more robust simulations will be needed to determine if the two results could agree with less than 10% difference and if over/under estimates could be reduced.

5.2 Angle Comparison with Slope Analysis

In addition to the individual analysis of each azimuthal position, a comparison of probe angles was performed. The purpose of this analysis is to discern the trends based on probe angle that are expected based on theory. Probes positioned at 0, 90, and 180 degrees point towards a rod gap and therefore should experience similar instantaneous pressures. Similarly, the probes at 45 and 135 degrees should yield similar results

because both point towards the center of a subchannel. A third comparison, 0 versus 45 degrees, was performed to determine the difference between a probe pointing to a gap and one pointing into a subchannel.

The results of these analyses are given two different ways: graphically and through a slope comparison.

5.2.1 Center of Subchannel (45 v. 135 degrees)

The probes at 45 and 135 degrees were plotted together using the simulated results from S1 and S2 and are provided in Figure 34. The 45 degree positions for S1 and S2 are represented by solid lines and the 135 degree positions for each simulation are plotted using dashed lines. Normalized pressure on the rod surface follows the same trend for both simulations and angles. Since mixing vane orientation is symmetric, the pressure is expected to be same for each probe pointed into the center of a subchannel. The only deviation between 45 and 135 degrees is the initial pressure at 0 hydraulic diameters. This is to be expected since this position is measured at the top of the grid strap, where the mixing vanes attach.

The CFD pressure results were plotted with the experimental results for the same two azimuthal positions in Figure 35. The experimental pressure is consistent between 45 and 135 degrees as it is for the CFD results. S1, S2, and the experimental results agree for the 45 and 135 degree positions, which validates the theory that pressure should be the same for all points facing into the subchannel.

In addition, the slopes for each angle were compared for S1, S2, and the experiment in Table 10. The slopes for S1 at each azimuthal position are identical. This

is expected since S1 was defined with a uniform velocity inlet. The pressure should be symmetric for all points facing into the subchannel due to grid symmetry. For S2 and the experiment, the slopes differed slightly between azimuthal positions. S2 was defined using a non-uniform velocity inlet to simulate the conditions of the experiment. It makes sense that pressure at the 45 and 145 degree positions is similar but not the same for these cases due to slight variations in the flow pattern.

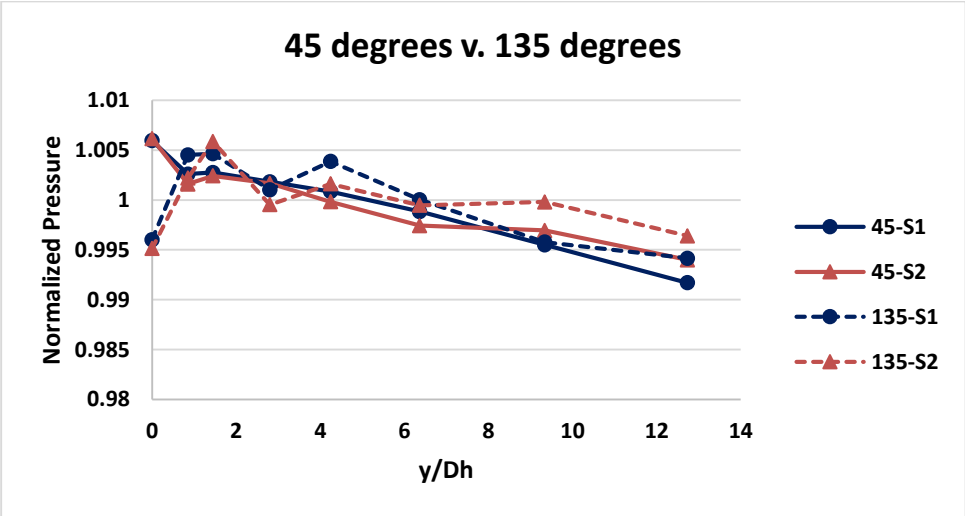

Figure 34: Comparison of normalized pressure for S1 and S2 at the rod surface for probes pointed into the center of a subchannel.

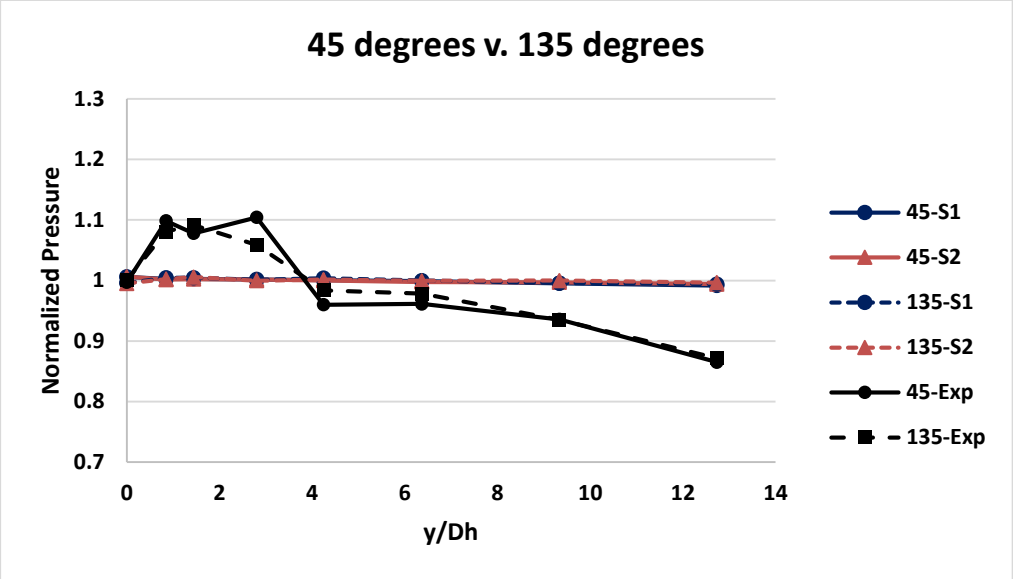

Figure 35: Comparison of CFD and experimental results for pressure probes pointed into the subchannel.

Table 10: Slope comparison between CFD and experiment for positions pointed into the subchannel.

	45 deg	135 deg
S1	-0.0009	-0.0009
S2	-0.0007	-0.0005
Experiment	-0.0198	-0.0181

5.2.2 Rod Gap (0 v. 90 v. 180 degrees)

The azimuthal positions pointed toward rod gaps were also compared. Pressure at 0, 90, and 180 degrees was plotted for S1 and S2 in Figure 36. The same trend in pressure exists for all angles pointed into rod gaps. This is not surprising because these positions are symmetrically the same, each pointing towards the position on the grid where the mixing vane originates.

The experimental pressure for the rod gap positions was plotted with the CFD results in Figure 37. There is slight variation in the trend of the pressure for each of the experimental azimuthal positions. Pressures at the 90 and 180 degree positions have the same trend with an average percent difference of 4%. The pressures at 0 degrees only agrees at certain points with the other two positions with an average percent difference of 8%. For all cases, the overall pressure remains relatively constant with a minor decrease in the streamwise direction. Since the vortices are primarily in the subchannels, there is not as strong as a pressure gradient at these points.

The slopes of the pressure change in the streamwise direction for the rod gap positions are given in Table 11. The slopes are identical between S1 and S2 for each azimuthal position. Since there is less flow variation in the rod gaps compared to the subchannels, the inlet velocity condition does not impact the change in pressure as it did for 45 and 90 degree positions. Also, the slope for the experimental pressures are not significantly different from the CFD results or between azimuthal positions.

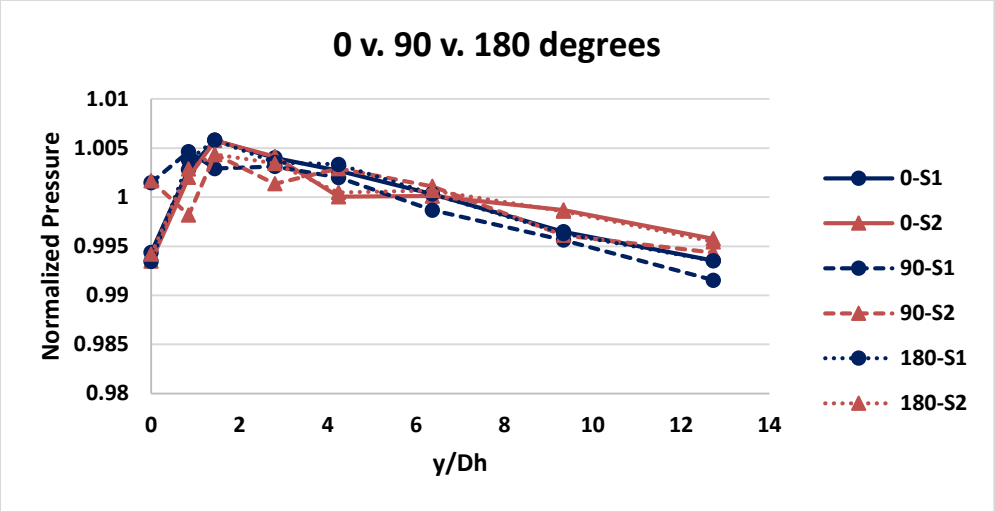

Figure 36: Comparison of S1 and S2 normalized pressure for azimuthal positions pointed toward a rod gap.

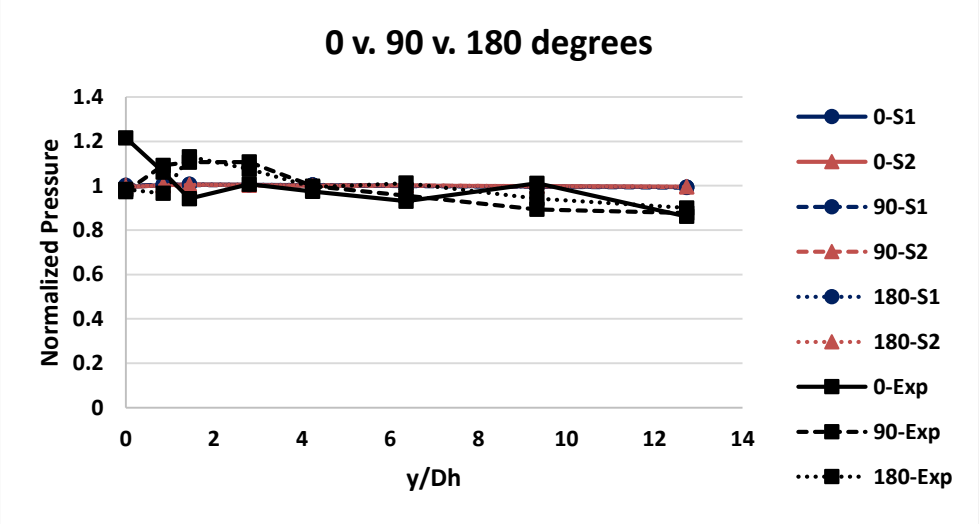

Figure 37: Comparison between CFD and experimental normalized pressures at the rod gap positions.

Table 11: Slope comparison between rod gap angles for S1, S2, and the experimental normalized pressures.

	0 deg	90 deg	180 deg
S1	-0.001	-0.001	-0.001
S2	-0.001	-0.001	-0.001
Experiment	-0.008	-0.022	-0.013

5.2.3 Center of Subchannel v. Rod Gap (0 v. 45 degrees)

The third azimuthal comparison is between a position pointed into a subchannel and one of the rod gap positions. The 0 and 45 degree positions were chosen for the purposes of this comparison and are plotted for S1 and S2 in Figure 38. Near the grid at a hydraulic diameter of 0, the two position types are dissimilar. As the flow progresses from 0 to 2 hydraulic diameters, the rod gap position pressure increases sharply, whereas the subchannel position decreases. From 2 hydraulic diameters until 13 hydraulic diameters, the rod gap and subchannel positions exhibit the same decreasing trend in pressure. This is due to the homogenization of the flow pattern downstream of the grid as the vortices lose energy and dissipate.

Experimental results were added to the CFD pressure results and plotted in Figure 39. As with the CFD results, the experimental pressure trend for the rod gap position and the subchannel position began differently. Unlike CFD, however, the rod gap position experienced a decrease in pressure from 0 to 2 hydraulic diameters and the subchannel position experience an increase. As the flow progressed further downstream, the rod gap and subchannel trends became similar. The slopes at each azimuthal position

for S1, S2, and the experimental results are given in Table 12. The CFD slopes are the same between simulations and for both angles, but the experimental slopes differ between 0 and 45 degrees. This could be due to slight variations in the experimental conditions that could not be simulated.

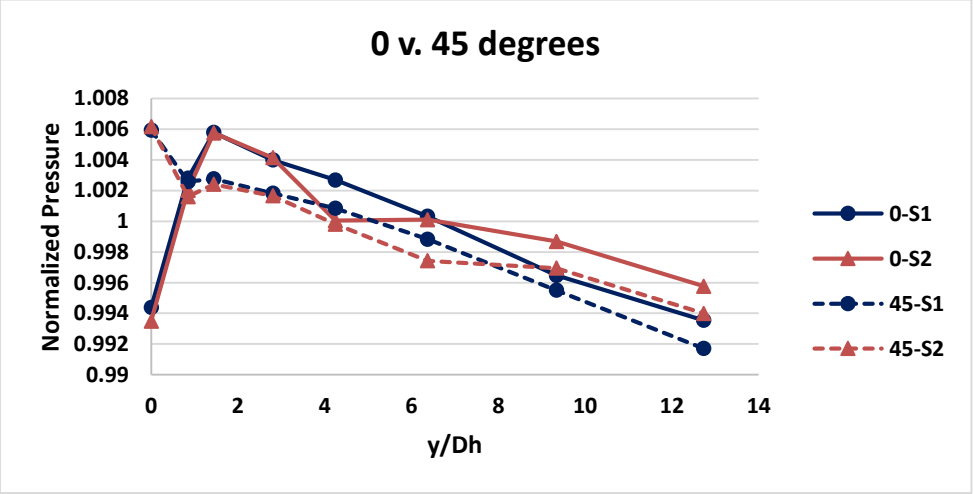

Figure 38: Comparison of normalized pressure between a probe facing into a subchannel and a probe pointed into a rod gap for S1 and S2.

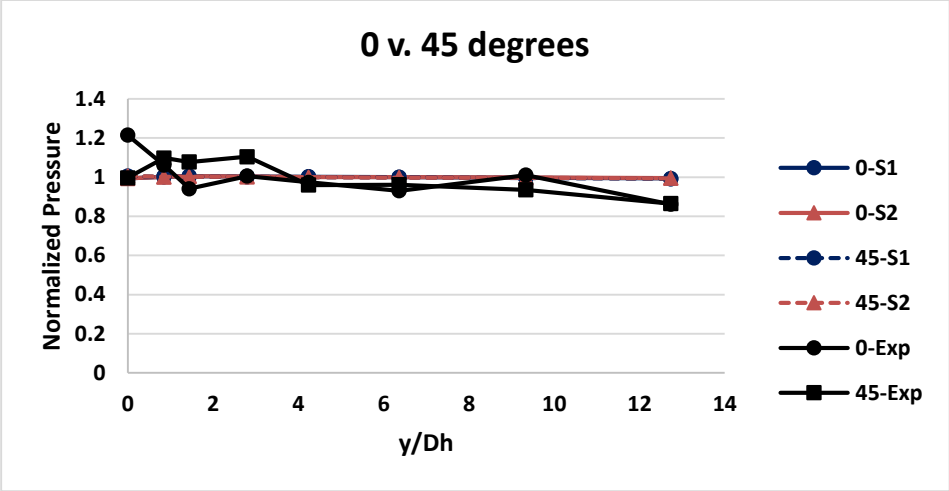

Figure 39: Comparison of rod gap and subchannel positions between CFD and experimental results.

Table 12: Slope comparison between rod gap and subchannel positions for S1, S2, and the experimental results.

	0 deg	45 deg
S1	-0.001	-0.001
S2	-0.001	-0.001
Experiment	-0.008	-0.020

5.2.4 Angle Comparison with Slope Analysis Summary

Similar azimuthal positions such as those pointed into a subchannel or rod gap were plotted together for the CFD and experimental data. In a comparison of S1 to S2 without experimental data, the two azimuthal positions pointed into the center of a

subchannel were similar except at the 0 mm axial position where a maximum exists for 45 degrees and a minimum for 135 degrees. This discrepancy was expected because at 45 degrees there is flow obstructed by a mixing vane directly in front of the probe whereas at 135 degrees this flow obstruction does not occur. This finding was not present in the experimental data, but that could be because the transducer is contained in a housing. Overall, the 45 and 135 degree positions for CFD and experimental data show the same axial trend featuring a peak in pressure near the grid and a dissipation of pressure further from the grid.

The CFD results at the rod gap locations of 0, 90, and 180 degrees also agreed in trend and were similar in magnitude. The main difference between the rod gap positions and the subchannel positions was the experimental comparison. The experimental rod gap positions experienced approximately the same magnitude of pressure as the CFD data and only a small pressure change occurs from 0 to 13 hydraulic diameters. The CFD subchannel position pressures were not on the same scale with the experimental data and there was a more pronounced peak in measured pressure at 45 and 135 degrees than at the measured positions of 0, 90, and 180 degrees. Overall, the CFD pressure probes yielded results that agree with intuition and exhibit trends similar to experimental results over the axial span.

6. CROSS-SECTIONAL PLANE ANALYSIS

This section provides a comparison of the CFD simulation results at a lateral plane 17 mm downstream of the mixing grid. The 17 mm axial distance was selected because the vortex effects close to the grid aid in a visual comparison. Use of one plane in this comparison was for the sake of brevity.

The initial hypothesis was that regardless of inlet velocity specification, uniform or non-uniform, both simulations should yield approximately the same results. The purpose of this analysis is to determine if the hypothesis is accurate for this type of problem.

6.1 Pressure Analysis

Absolute pressure was recorded for simulations S1 and S2. In order to compare results despite the difference in inlet conditions, the absolute pressure results from both simulations were normalized by surface averaged absolute pressure of the inlet. Pressure magnitude was plotted in STAR-CCM+ for both CFD simulations 17 mm downstream of the grid. The results are presented in Figure 40.

The normalized absolute pressure results from S1 appear uniform across the lateral plane. This makes sense because the inlet condition of S1 was defined using uniform velocity. The results from S2, however, display variations in pressure across the plane. This is because the inlet for S2 was defined using a non-uniform velocity profile. The variation between the two simulations means that the hypothesis is incorrect.

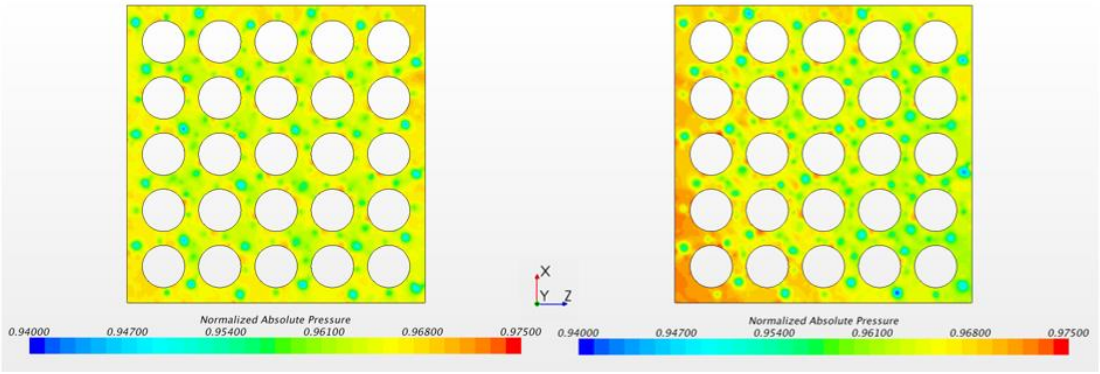

Figure 40: S1 (left) and S2 (right) normalized absolute pressure across the plane 17 mm downstream of the top grid strap.

6.2 Velocity Plane Analysis

To compare the tangential vector velocity of simulations S1 and S2, the vectors on each lateral plane were normalized by 2.48 m/s, the uniform velocity inlet condition of S1. The velocity results of both simulations for the four subchannels surrounding the central rod are provided in Figure 41.

The tangential velocity vectors from the S1 results have a lower magnitude than those from S2 in the four subchannels. This is evidence that cross flow, particularly in the vortices, is greater due to the non-uniform velocity inlet condition applied to S2. Additionally, the S1 vector field is more uniform than the S2 field because of the inlet condition.

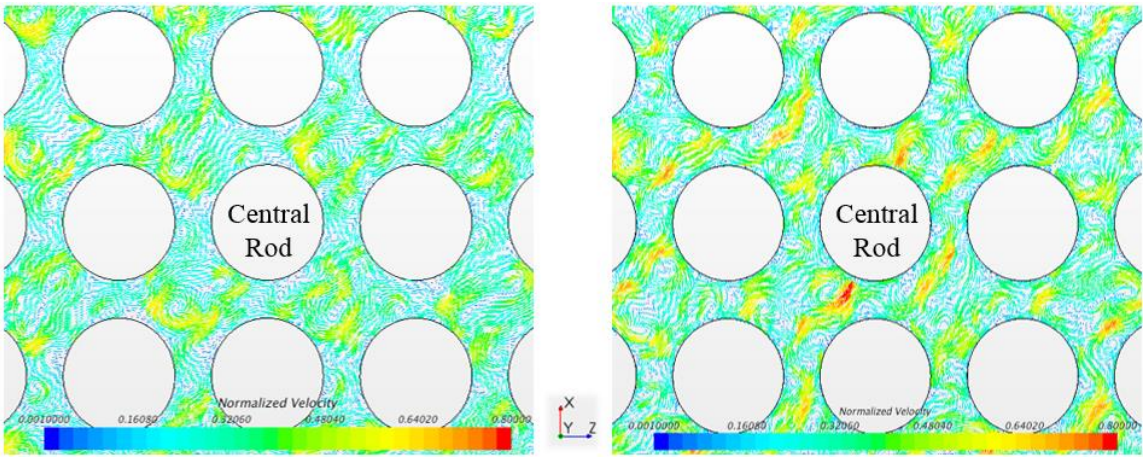

Figure 41: S1 (left) and S2 (right) normalized tangential velocity vectors across the plane 17 mm downstream of the top grid strap.

6.2.1 Velocity Plane Analysis

As part of this research, the effect of the flow housing walls was also qualitatively analyzed. The subchannels one row in from the wall are not uniform between subchannels. The four middle subchannels are symmetrical and more uniform than those closer to the bundle exterior. This was the reason why a 5 x 5 bundle was chosen over a smaller geometry in an effort to further reduce the wall effect on the subchannels of interest.

7. CFD VELOCITY VECTOR ANALYSIS

An additional analysis in this work is to study the CFD results when processed using the same method as experimental PIV data. By processing the CFD vector data in the same manner as PIV data, the ground work is laid to benchmark CFD and PIV. As an additional benefit, this analysis procedure reduces the CFD vector data down to a more manageable data set which is easier to visualize.

7.1 MATLAB Pre-processes

As with the experimental data, the raw form of the CFD data was not in a form conducive to the analysis procedure. Each CFD data file was exported from STAR-CCM+ with ".csv" formatting and columns arranged alphabetically. Consequently, all the data files had x, y, and z coordinates listed in the last three columns instead of the first three. The filtering program, discussed in Section 7.2, only reads data in a prescribed order: x, y, u, v. The purpose of the MATLAB script is to read in the ".csv" formatted CFD data, write only the pertinent data for the plane to a matrix, and export the matrix to a ".txt" file format. Each converted data file contains four columns: x, z, u, w for lateral planes and x, y, u, v for axial planes.

7.2 TAMU PTV Filtering

The TAMU PTV (Particle Tracking Algorithm) filtering code was used for the CFD velocity data reduction and is the same code used to reduce PIV experimental data.

While the code has many functions that are beyond the scope of this work, the filtering function adequately reduces CFD velocity data from a fine mesh to a coarse mesh that can be compared one to one with PIV.

The code reads in text data files organized in x, y, u, v columns and averages the vectors from many time steps into one vector field. Additionally, the filtering code converts the fine vector field obtained from CFD into a coarser field by averaging the vectors in neighboring cells to form a larger cell with two representative vectors. This process was performed for the lateral and axial CFD planes. Figure 42 shows the general and filter settings used for the lateral planes and Figure 43 gives the axial plane general and filter settings.

In the lateral and axial filtering settings, the input dimensions reference each plane origin where xmin is the portion in the negative x, xmax is the dimension in the positive x-direction, ymin is the dimension in the negative y-direction, and ymax is the dimension in the positive y-direction.

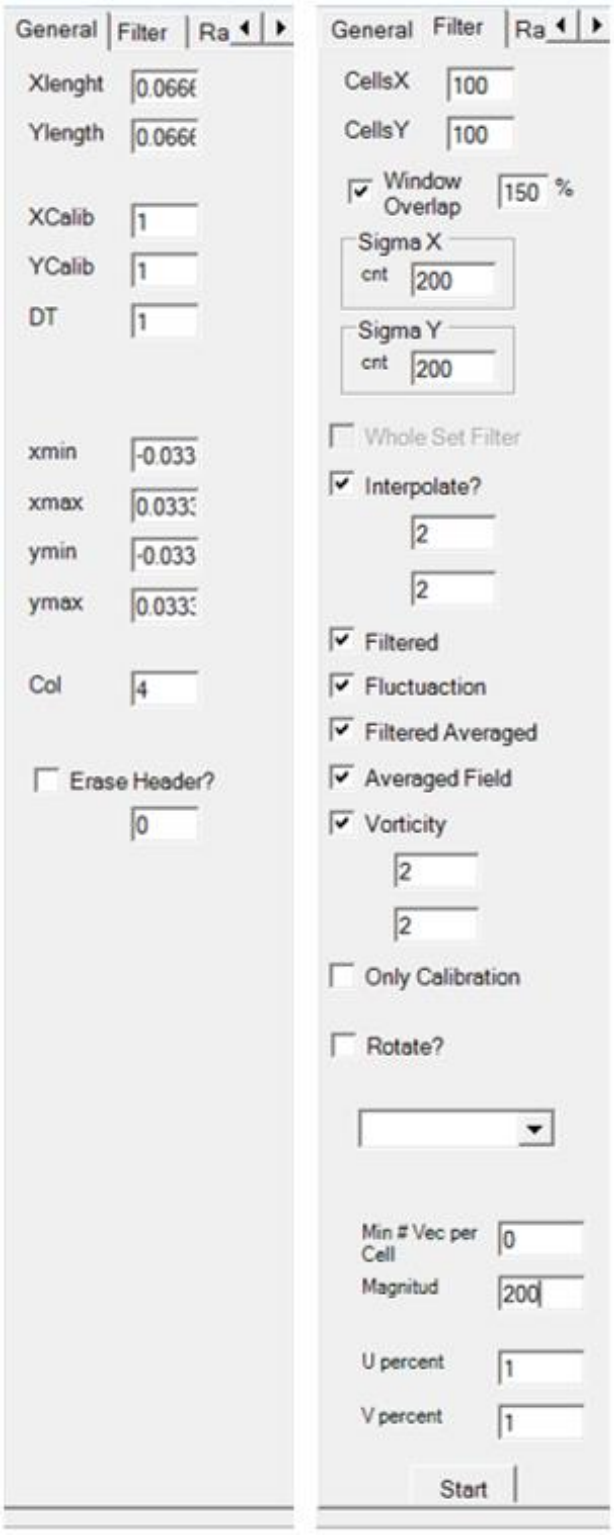

Figure 42: General and filter setting for all lateral planes.

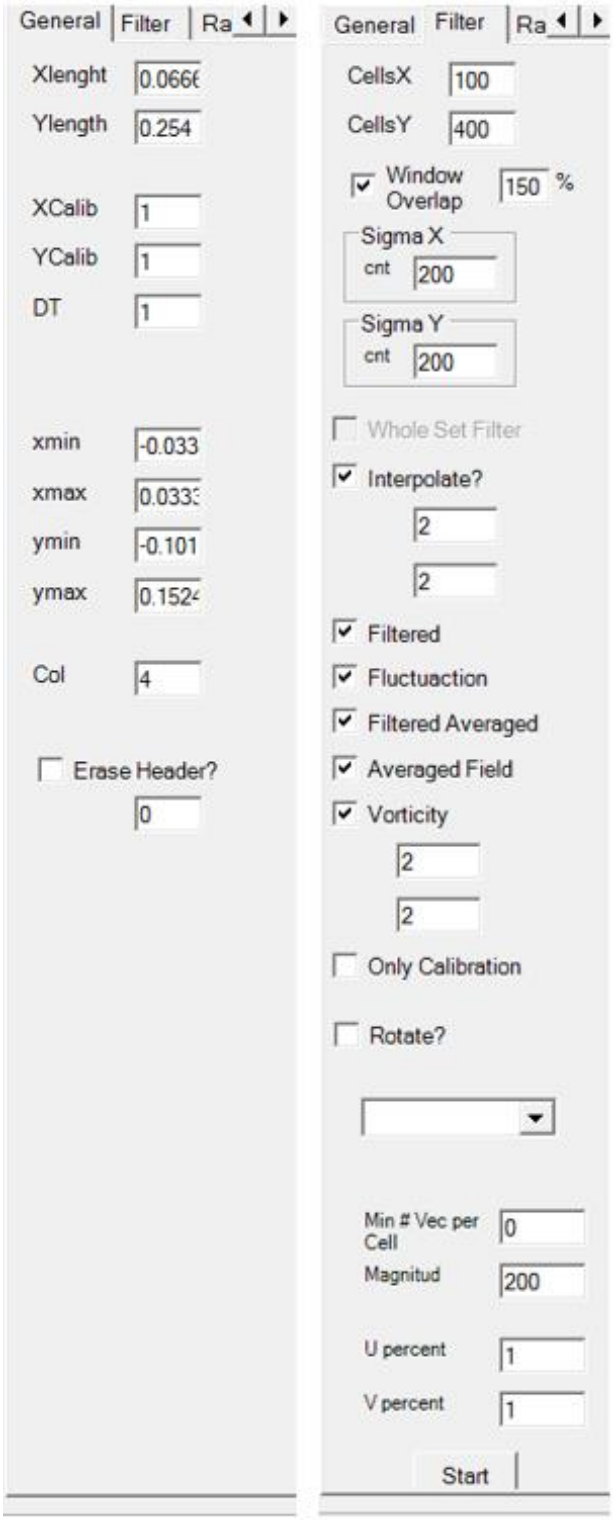

Figure 43: General and filter settings for all axial planes.

7.3 Results

In this section, the CFD data that was filtered using PTV will be compared to the original, full-resolution CFD results. It is important to compare the filtered CFD velocity vectors with the original CFD data to determine if filtering maintains the integrity of the results. The conclusions derived in this section will determine if filtering using PTV is an appropriate method to reduce CFD data for comparison with PIV data.

Five lateral planes were selected for the comparison: 1 hydraulic diameter upstream, 17 mm, 33 mm, 50 mm, and 110 mm downstream of the mixing grid. These planes were selected because of their distinctive vortex characteristics. At each plane, S1 was compared to S2 results and filtered was compared to unfiltered results for the four subchannels surrounding the central rod. The four subchannels used in this analysis are designated by boxes in Figure 44. A relative vector length, grid units divided by magnitude, of 0.28 was used defined for all planes except 1 hydraulic diameter upstream, which used a relative vector length of 2.6 in order to visualize the vectors.

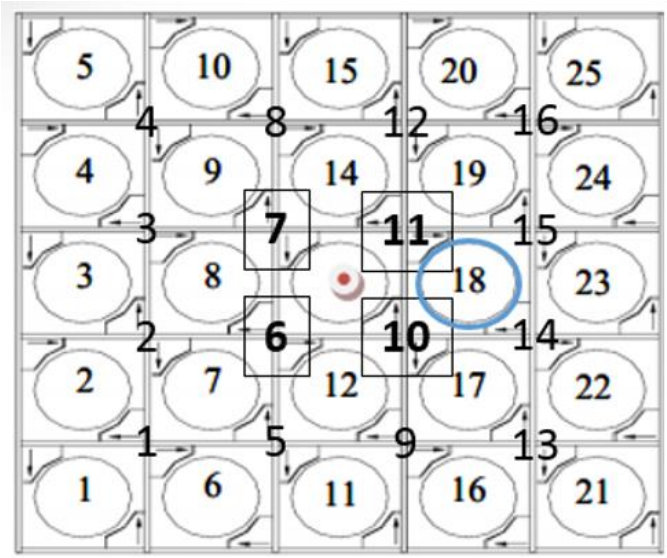

Figure 44: Schematic showing the relative location of the four subchannels of interest. These subchannels are 6, 7, 10, and 11 and are outlined using boxes.

7.3.1 Lateral 1 Hydraulic Diameter Upstream

The first plane of interest is the plane 1 hydraulic diameter upstream of the grid. This plane is important for determining the velocity field characteristics before the flow passes through the grid. The vector fields of the original, unfiltered CFD data and the filtered data are provided in Figure 45 for S1 and S2. The unfiltered vector field is much denser than the filtered results because it corresponds to the fine mesh of the CFD simulation. In the case of the filtered data, vectors from the unfiltered mesh were averaged to create a coarse mesh that is 100 x 100 cells.

The S1 vector fields are the same between the unfiltered and filtered plots. Vectors are uniformly distributed with the majority pointed out of the page, which is

expected in the portion of the fuel assembly just prior to a mixing grid. The S2 vector field exhibits more cross flow than S1 because of the non-uniform velocity inlet condition. Flow is driven more preferentially from one subchannel to another to compensate for the pressure gradient. In both simulations, no vortices are visible which is expected at this axial elevation.

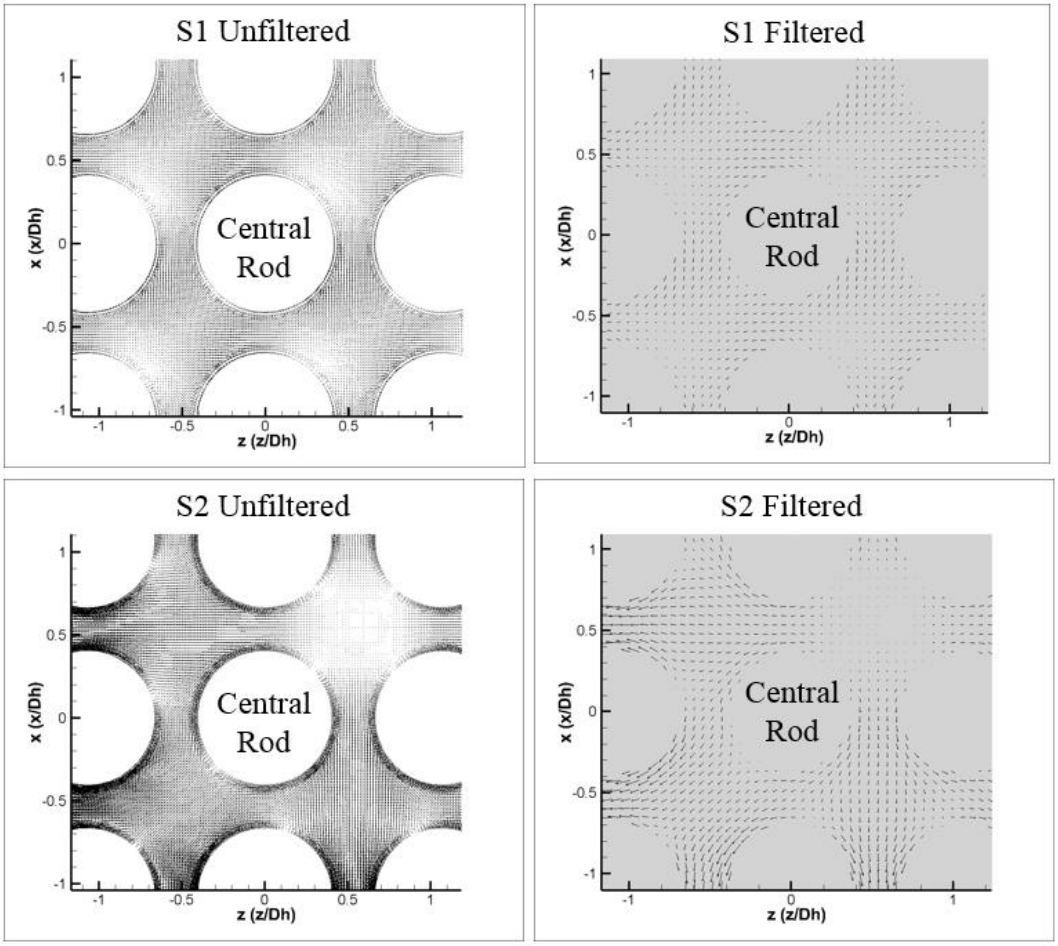

Figure 45: Unfiltered (left) and filtered (right) normalized velocity vector field for S1 (up) and S2 (down) one hydraulic diameter upstream of the grid.

7.3.2 Lateral 17 mm Downstream

The next lateral plane is positioned at 17 mm downstream of the mixing grid. The expectation at this position is to be able to decipher four vertices per subchannel and larger magnitude vectors throughout the field. The four subchannels results from S1 and S2 for the unfiltered and filtered cases are provided in Figure 46. Four vortices are present in the S1 and S2 cases, but the S2 primary vortices are more stretched than in S1. Once again, the non-uniform inlet velocity condition leads to more cross flow between subchannels.

The unfiltered and filtered fields show approximately the same pertinent details, with the exception of the smaller secondary vortices at the edges of the subchannels. These smaller vortices are present in the filtered plots, but are not as discernable. However, one advantage to the lower resolution of the filtered data is the ability to visualize the streamlines from one subchannel to the next. The high vector density of the unfiltered data is better for vortex identification, but flow characteristics from subchannel to subchannel across the plane can more easily be seen using less resolution.

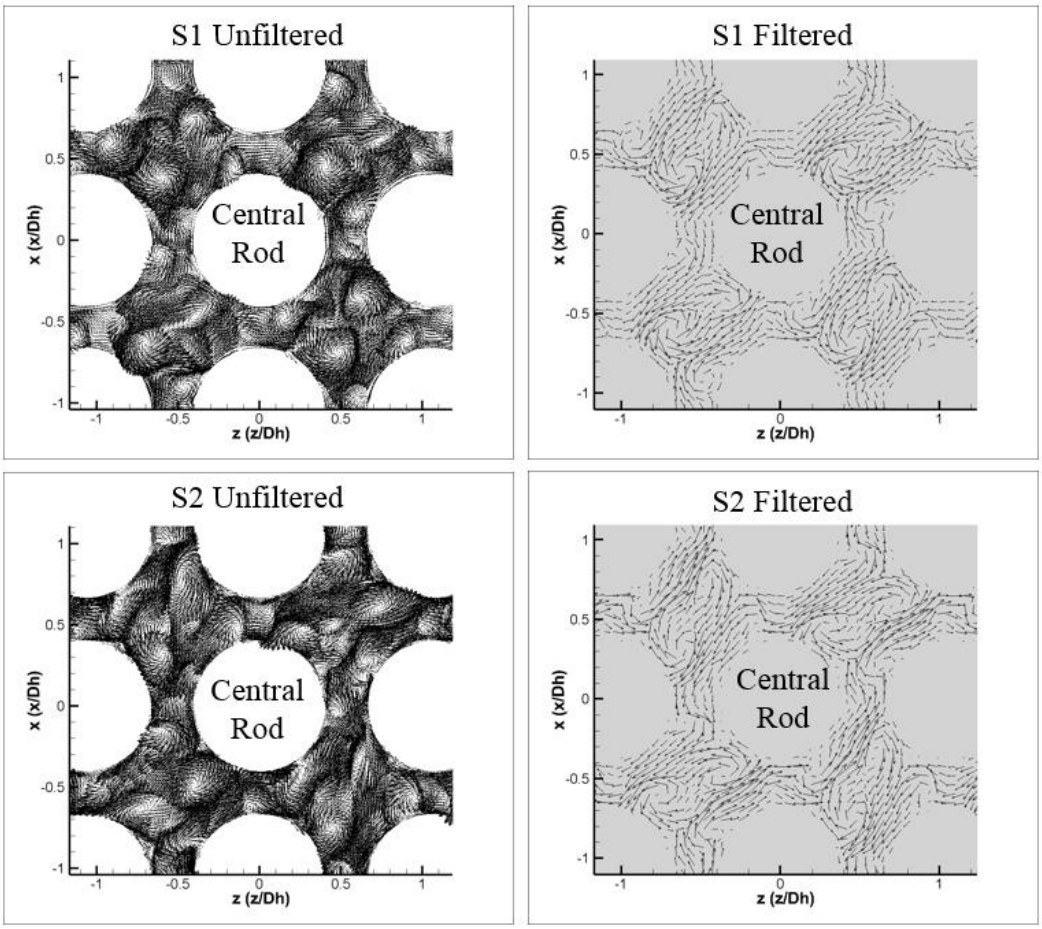

Figure 46: Unfiltered (left) and filtered (right) normalized velocity vector field for S1 (up) and S2 (down) 17 mm downstream of the grid.

7.3.3 Lateral 33 mm Downstream

At 33 mm downstream, the number of vortices in each subchannel decreases to about 2 to 3 as the flow becomes more organized. The four central subchannels for each case 33 mm downstream of the mixing grid are given in Figure 47. At this lateral position, the vortices are more discernable for S1 than S2. In S1, the vortices are transitioning to a more ordered, circular form. The vortices in S2 are becoming less

prominent and moving towards the corners of the subchannel. The filtered results are a generality of these trends. With fewer vectors, it the primary vortices are easier to identify, especially in S2 where the vortices have shifted to the corners. The disadvantage of the filtered plots is the loss of any minor vortices at the edges or in the gaps.

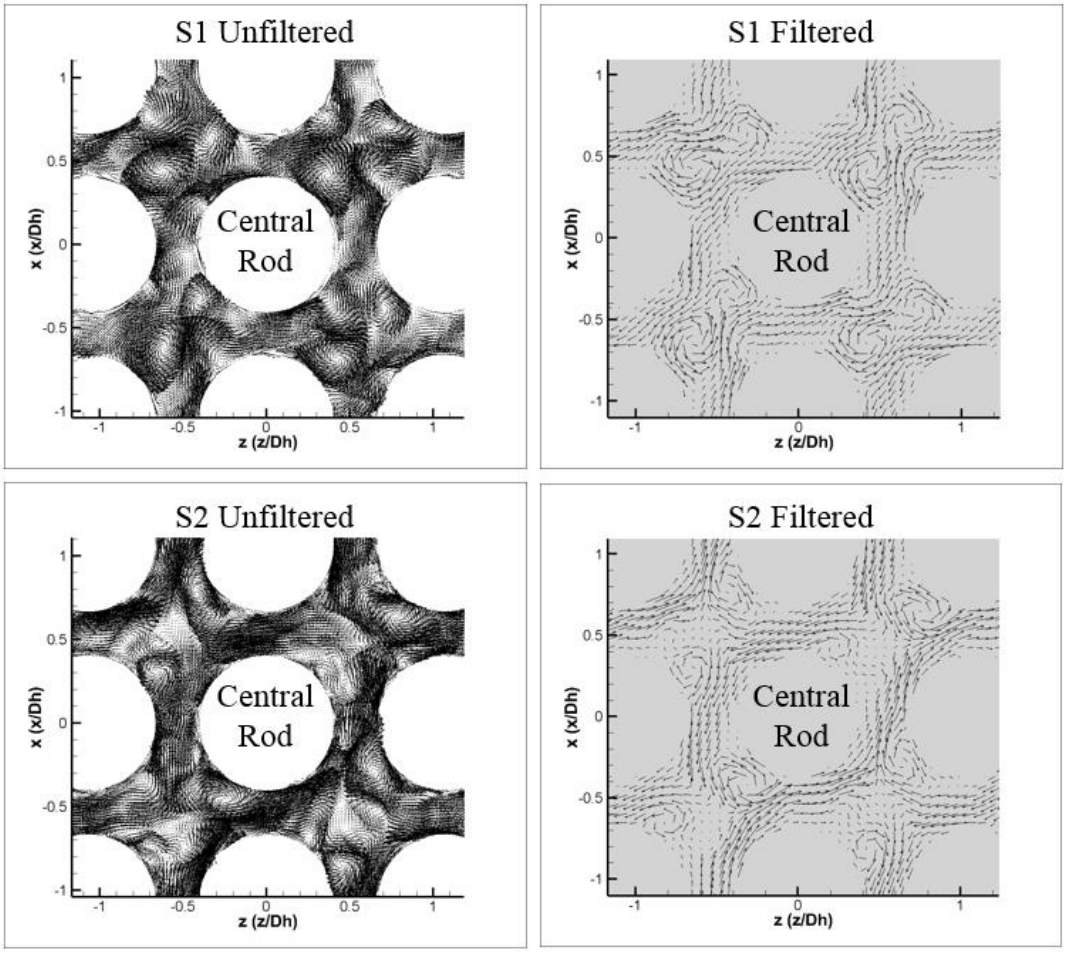

Figure 47: Unfiltered (left) and filtered (right) normalized velocity vector field for S1 (up) and S2 (down) 33 mm downstream of the grid.

7.3.4 Lateral 50 mm Downstream

At a distance of 50 mm from the grid, the expectation is to visualize the two primary vortices combining together to form one vortex. The four cases for each subchannel at 50 mm are provided in Figure 48. Once again, the S1 vector field appears more uniform than S2. Each subchannel shows the combination process enveloping the entirety of the subchannel for S1, In S2, the vortices are in the corners and the streamlines between each subchannel are more prominent.

The filtered plots are similar to the high resolution unfiltered plots, except that for S1, the combination process is not as pronounced. In each subchannel it appears as though there is one large vortex instead of a combination of two. The S2 filtered plot is the same as the unfiltered, but the streamlines are more noticeable than with higher resolution.

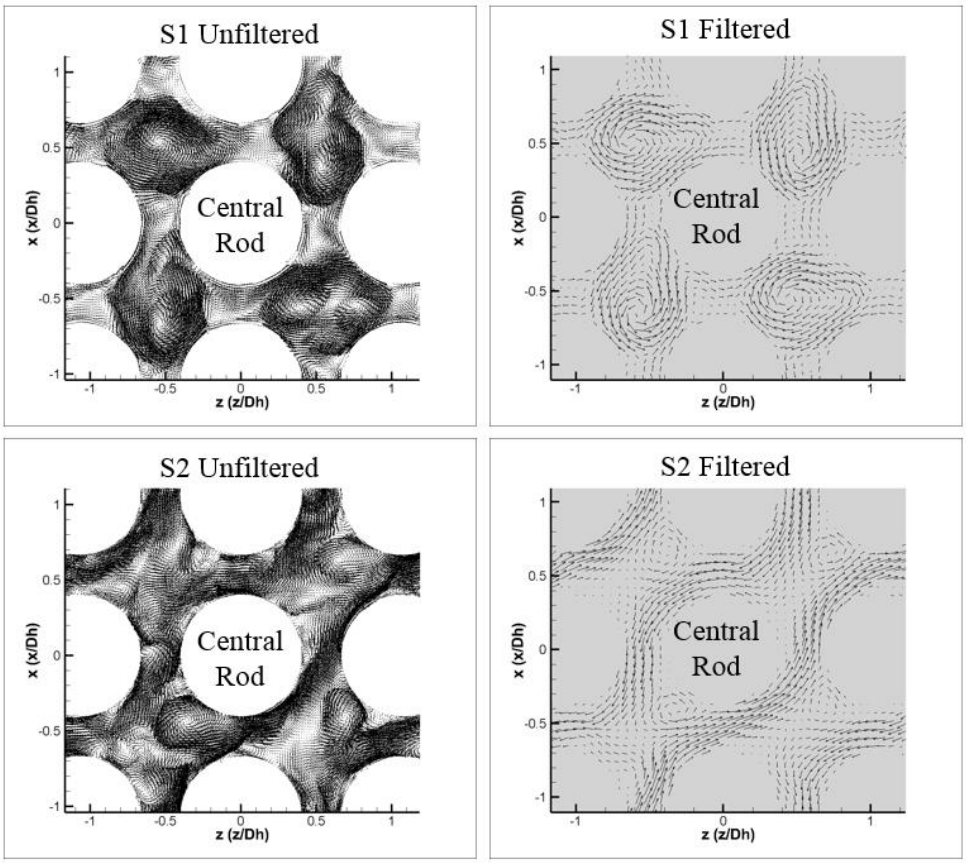

Figure 48: Unfiltered (left) and filtered (right) normalized velocity vector field for S1 (up) and S2 (down) 50 mm downstream of the grid.

7.3.5 Lateral 110 mm Downstream

The last plane of interest is positioned 110 mm downstream of the mixing grid. At this distance, the expectation is to visualize one large vortex in each subchannel. The plots of the four subchannels for each case is presented in Figure 49.

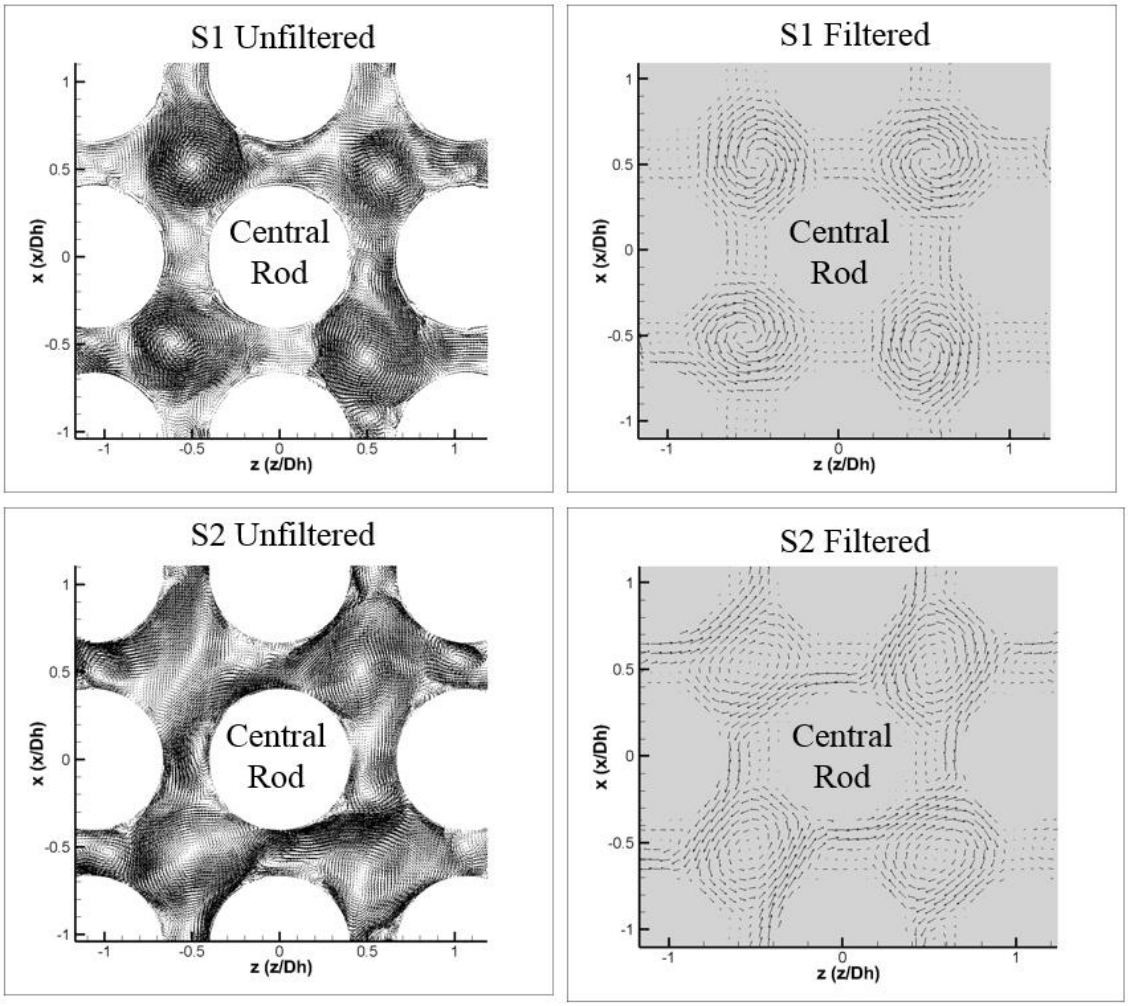

Figure 49: Unfiltered (left) and filtered (right) normalized velocity vector field for S1 (up) and S2 (down) 110 mm downstream of the grid.

S1 and S2 exhibit the large vortex that was expected in each subchannel. The vectors within the vortices of S1 appear larger in magnitude than those in S2, but S2 has higher cross flow velocity that streamlines from one subchannel to the next. The same trend is reflected in the filtered data. The higher magnitude velocity vectors are within

the vortex for S1, whereas for S2 the larger vectors are near the edges of the subchannel as flow passes from one subchannel to the next.

The side-by-side comparison of S1 and S2 for all five planes demonstrated that the uniform and non-uniform velocity inlet conditions before the grid provide fundamentally different results. The amount of cross flow is higher in S2, as well as energy dissipation. Additionally, while the velocity fields from S1 represent the theoretically expected results, the vector fields obtained from S2 are more similar to the experimental PIV data that was taken in the past.

The comparison between unfiltered and filtered vector fields confirms that the vital flow structures are maintained when the vector field resolution is reduced. This finding will allow one-to-one comparisons between experimentally measured PIV data and CFD, where the resolution is equivalent between the two data sets.

7.3.6 CFD Velocity Vector Analysis Summary

The second CFD simulation was performed to determine the validity of the initial hypothesis that a uniform velocity inlet could be used in place of a non-uniform inlet condition for this type of problem. It was initially assumed that the two simulations would yield approximately the same results. Through this analysis, it was discovered that the non-uniform inlet velocity condition yields different results than the constant velocity condition. On average, both simulations produced the theoretically expected number of vortices per subchannel: 4 are present at 1.44 hydraulic diameters from the grid, 2 are present at 2.8 hydraulic diameters, and 1 is present from 4.2 to 12.7 hydraulic diameters. A discrepancy in number of vortices exists between S1 and S2 at 4.2

hydraulic diameters downstream of the grid. This result was expected because this axial distance is a transition zone where the 2 vortices are combining to form 1 vortex that will continue downstream until it dissipates. When analyzing the flow pattern over time, S1 displays 1 or 2 vortices whereas S2 only has 1 dominant vortex.

Another key difference between the flow structures of S1 and S2 is vortex shape. The vortices in S1 are circular throughout the simulated axial domain, whereas the S2 vortices are more elliptic. Also, the S2 vortices are closer to the subchannel boundaries instead of being in the center of the subchannel like S1. More cross flow was observed in S2 throughout the simulated axial domain than S1, which is similar to previous experimental observations using PIV. The most interesting observation in this analysis of inlet velocity condition was that the flow appears to retain memory of the inlet boundary condition well after the turbulent effects from the mixing vanes begin to dissipate. This implies that defining the inlet velocity properly is vital for this type of problem and should be considered in all future simulations.

8. CONCLUSIONS

Instantaneous pressure measurements were collected experimentally at the Texas A&M Advanced Optical Multiphase Flow Research Laboratory using pressure transducers installed within an instrumented rod. In addition, a Computational Fluid Dynamics (CFD) simulation, S1, was generated at the Westinghouse Electric Company Fuel Fabrication Facility in Columbia, SC using a uniform velocity inlet condition. An additional simulation, S2, was performed at Texas A&M with a non-uniform velocity inlet condition to determine the validity of the uniform inlet velocity assumption. The results from both simulations were compared with the experimental measurements and confirm that overall CFD can provide similar results as experiments. Instantaneous pressures obtained from the two CFD simulations agreed with the experimental data within 10%, however, the two simulations under-predicted pressures compared to experiments. Further testing and more robust simulations will be needed to determine if the two results could agree with less than 10% difference and if the underestimates could be reduced.

A slope and angle analysis was also performed for both CFD simulations and the experimental pressure data. Similar azimuthal positions such as those pointed into a subchannel or rod gap were plotted together for the CFD and experimental data. In a comparison of S1 to S2 without experimental data, the two azimuthal positions pointed into the center of a subchannel were similar except at the 0 mm axial position where a maximum exists for 45 degrees and a minimum for 135 degrees. This discrepancy was

expected because at 45 degrees there is flow obstructed by a mixing vane directly in front of the probe whereas at 135 degrees this flow obstruction does not occur. This finding was not present in the experimental data, but that could be because the transducer is contained in a housing. Overall, the 45 and 135 degree positions for CFD and experimental data show the same axial trend featuring a peak in pressure near the grid and a dissipation of pressure further from the grid.

The CFD results at the rod gap locations of 0, 90, and 180 degrees also agreed in trend and were similar in magnitude. The main difference between the rod gap positions and the subchannel positions was the experimental comparison. The experimental rod gap positions experienced approximately the same magnitude of pressure as the CFD data and only a small pressure change occurs from 0 to 13 hydraulic diameters. The CFD subchannel position pressures were not on the same scale with the experimental data and there was a more pronounced peak in measured pressure at 45 and 135 degrees than at the measured positions of 0, 90, and 180 degrees. Overall, the CFD pressure probes yielded results that agree with intuition and exhibit trends similar to experimental results over the axial span.

The second CFD simulation was performed to determine the validity of the initial hypothesis that a uniform velocity inlet could be used in place of a non-uniform inlet condition for this type of problem. It was initially assumed that the two simulations would yield approximately the same results. Through this analysis, it was discovered that the non-uniform inlet velocity condition yields different results than the constant velocity condition. On average, both simulations produced the theoretically expected

number of vortices per subchannel: 4 are present at 1.44 hydraulic diameters from the grid, 2 are present at 2.8 hydraulic diameters, and 1 is present from 4.2 to 12.7 hydraulic diameters. A discrepancy in number of vortices exists between S1 and S2 at 4.2 hydraulic diameters downstream of the grid. This result was expected because this axial distance is a transition zone where the 2 vortices are combining to form 1 vortex that will continue downstream until it dissipates. When analyzing the flow pattern over time, S1 displays 1 or 2 vortices whereas S2 only has 1 dominant vortex.

Another key difference between the flow structures of S1 and S2 is vortex shape. The vortices in S1 are circular throughout the simulated axial domain, whereas the S2 vortices are more elliptic. Also, the S2 vortices are closer to the subchannel boundaries instead of being in the center of the subchannel like S1. More cross flow was observed in S2 throughout the simulated axial domain than S1, which is similar to previous experimental observations using PIV. The most interesting observation in this analysis of inlet velocity condition was that the flow appears to retain memory of the inlet boundary condition well after the turbulent effects from the mixing vanes begin to dissipate. This implies that defining the inlet velocity properly is vital for this type of problem and should be considered in all future simulations.

As part of this research, the effect of the flow housing walls was also qualitatively analyzed. The subchannels one row in from the wall are not uniform between subchannels. The four middle subchannels are symmetrical and more uniform than those closer to the bundle exterior. This was the reason why a 5 x 5 bundle was

chosen over a smaller geometry in an effort to further reduce the wall effect on the subchannels of interest.

Velocity vectors from the two CFD simulations were reduced to the resolution of experimental PIV measurements. The purpose was to prove that reducing vector field resolution does not lose meaningful data. Through side-by-side comparison, it was determined that this process does not remove the pertinent flow structures and will provide a means to benchmark PIV results to CFD using the same resolution.

9. RECOMMENDATIONS AND FUTURE WORK

To complete this analysis, a full error analysis must be performed on the experiment. This includes performing a test of the transducers to determine if they are sensing the correct signal. Additionally, the CFD simulation geometry should be expanded to reflect the axial length of the experiment. The benefit to a full length model is the ability to compare the region just upstream of the grid to the region that is just before the next grid. The results should be similar at these two regions.

The biggest area for future work is the velocity comparison to PIV. The groundwork for this analysis was initiated in this work, but should be expanded to include a detailed CFD comparison to PIV experimental data as well as a wavelet analysis comparison.

REFERENCES

[1] N. Park, H. Rhee, J. Park, S. Jeon and H. Kim, "Indirect estimation method of the turbulence induced fluid force spectrum acting on a fuel rod," *Nuclear Engineering and Design,* vol. 239, no. 7, pp. 1237-1245, 2009.

[2] K. Kim, "The study on grid-to-rod fretting wear models for PWR fuel," *Nuclear Engineering and Design,* vol. 239, no. 12, pp. 2820-2824, 2009.

[3] M. J. Pettigrew, L. N. Carlucci, C. E. Taylor and N. J. Fisher, "Flow induced vibration and related technologies in nuclear components," *Nuclear Engineering and Design,* vol. 131, no. 1, pp. 81-100, 1991.

[4] A. Horvath and B. Dressel, "Numerical simulations of square arrayed rod bundles," *Nuclear Engineering and Design,* vol. 247, pp. 168-182, 2012.

[5] C. C. Liu, Y. M. Ferng and C. K. Shih, "CFD evaluation of turbulence models for flow simulation of the fuel rod bundle with a spacer assembly," *Applied Thermal Engineering,* vol. 40, pp. 389-396, 2012.

[6] K. Podila, Y. F. Rao, M. Krause and J. Bailey, "A CFD simulation of 5 x 5 rod bundles with split-type spacers," *Progress in Nuclear Engineering,* vol. 70, pp. 167-175, 2014.

[7] A. Hatman, G. Williams, M. Martin, T. Keheley, C. Lascar, K. Goodheart and A. Chatelain, "CFD analysis of reactor core flow field in support of FIV diagnosis," in *The 15th International Topical Meeting on Nuclear Reactor Thermal-Hydraulics,* Pisa, Italy, 2013.

[8] A. M. Elmahdi, R. Lu, M. E. Conner, Z. E. Karoutas and E. Baglietto, "Flow induced vibration forces on a fuel rod by LES CFD analysis," in *The 14th International Topical Meeting on Nuclear Reactor Thermal-Hydraulics,* Toronto, Ontario, Canada, 2011.

[9] J. Bakosi, M. A. Christon, R. B. Lowrie, L. A. Pritchett-Sheats and R. R. Nourgaliev, "Large-eddy simulations of turbulent flow for grid-to-rod fretting in nuclear reactors," *Nuclear Engineering and Design,* vol. 262, pp. 544-561, 2013.

[10] T. Ikeno and T. Kajishima, "Decay of swirling turbulent flow in rod-bundle," *Journal of Fluid Science and Technology,* vol. 1, no. 1, pp. 36-47, 2006.

[11] S. Delafontaine and G. Ricciardi, "Fluctuating pressure calculations induced by axial flow through mixing grid," *Nuclear Engineering and Design,* vol. 242, pp. 233-246, 2012.

[12] P. Moussou, S. Benhamadouche and C. Bodel, "CFD estimation of the unsteady fluid force along a fuel rod downstream of a mixing grid," in *ASME 2011 Pressure Vessels and Piping Conference*, Baltimore, Maryland, 2011.

[13] S. K. Chang, S. K. Moon, W. P. Baek and Y. D. Choi, "Phenomenological investigations on the turbulent flow structures in a rod bundle array with mixing devices," *Nuclear Engineering and Design,* vol. 238, no. 3, pp. 600-609, 2008.

[14] E. E. Dominguez-Ontiveros, Y. A. Hassan, M. E. Conner and Z. E. Karoutas, "Experimental benchmark data for PWR rod bundle with spacer-grids," *Nuclear Engineering and Design,* vol. 253, pp. 396-405, 2012.

[15] K. M. Kim, B. I. Lee, D. Lee, H. H. Cho and K. H. Jeong, "Experimental and numerical study on local pressure distributions in a system-integrated modular reactor," *Annals of Nuclear Energy,* vol. 47, pp. 216-224, 2012.

[16] M. E. Conner, E. Baglietto and A. M. Elmahdi, "CFD methodology and validation for single-phase flow in PWR fuel assemblies," *Nuclear Engineering and Design,* vol. 240, no. 9, pp. 2088-2095, 2010.

[17] M. E. Conner, Y. A. Hassan and E. E. Dominguez-Ontiveros, "Hydraulic benchmark data for PWR mixing vane grid," *Nuclear Engineering and Design,* vol. 264, pp. 97-102, 2013.

[18] J. Yan, M. E. Conner, R. A. Brewster, Z. E. Karoutas, E. E. Dominguez-Ontiveros and Y. A. Hassan, "Validation of CFD method in predicting steady and transient flow field generated by PWR mixing vane grid," in *CFD4NRS-4-The Experimental Validation and Application of CFD and CMFD Codes in Nuclear Reactor Technology, OECD/NEA & International Atomic Energy Agency (IAEA) Workshop*, Daejeon, Korea, 2012.

[19] H. L. McClusky, M. V. Holloway, T. A. Conover, D. E. Beasley, M. E. Conner and L. D. Smith III, "Mapping of the Lateral Flow Field in Typical Subchannels of a Support Grid with Vanes," *Journal of Fluids Engineering,* pp. 987-996, 2003.

[20] P. J. Roache, "Systematic Grid Convergence Studies and the Grid Convergence Index," in *Verification and Validation in Computational Science and Engineering*, Albuquerque, New Mexico, Hermosa Publishers, 1998, pp. 107-135.

APPENDIX

```
%%%%%%%%%%%%%%%%%%%%%%%%%%%%%%%%%%%%InstantaneousPressure.M%%%%%%%%%%%%%%%%%%%%%%%
% Find and Open file containing list of file names
pth='E:\Natalie_Experimental\050714\'; %[Paste directory path]
name1='180degrees.txt';            %[Paste directory names containing the files to process]

nsamples=16;                        %Number of files to open

% Open file to read from [filenames.txt]
fid1 = fopen([pth,name1]);
count=0;
scA1=zeros(nsamples,8);
tline1 = fgetl(fid1);

% Loop through each directory in name1
while ischar(tline1);
    disp(tline1);
    count=count+1;

  % Import the file. This file should be the exported file from the NI DAQ
  % system. copy the address of the file
  newData1 = importdata([pth,tline1,'\Custom_Voltage.txt'],'\t',7);
  noheader1=newData1.data;

  % Collect voltage data by sensor (each column)
    ch0 = noheader1(:,1);
    ch1 = noheader1(:,2);
    ch2 = noheader1(:,3);
    ch3 = noheader1(:,4);
    ch4 = noheader1(:,5);
    ch5 = noheader1(:,6);
    ch6 = noheader1(:,7);
    ch7 = noheader1(:,8);

  % Convert voltage to pressure
  % Area, lb, and N can be used to convert pressure to force
    % Area = surface area of the mini pressure transducers
```

Figure A.1: MATLAB script used to pre-process experimental data (see chapter 2). This is part 1 of 5. This script is used to convert instantaneous voltage to instantaneous pressure based on the pressure transducer calibration equations that were obtained based on sensor specifics and an experimental calibration of the sensor using hydrostatic measurements. The read and output files are all in text format for use with multiple programs. The pressure conversion equations are contained in a while loop and each set of equations is specific to the azimuthal position of the sensor. For each run of the script, the extraneous azimuthal positions are commented out so that the only set of equations being calculated are those pertaining to the azimuthal position of interest.

```
  % lb = pound force (P*A=0.04382)
  % N = Newtons (lbf*4.44822)
  % Area = 0.04382;
  % toN = 4.44822;
    % Initialization of variables for each sensor in for loops
    psi0 = zeros(length(ch4),1);
    psi1 = zeros(length(ch4),1);
    psi2 = zeros(length(ch4),1);
    psi3 = zeros(length(ch4),1);
    psi4 = zeros(length(ch4),1);
    psi5 = zeros(length(ch4),1);
    psi6 = zeros(length(ch4),1);
    psi7 = zeros(length(ch4),1);

    % 0 degrees
%         for i = 1:length(ch4)
%             % ch0 (0-30 psig)
%             psi0(i,:) = (6.0216*ch0(i,:)-0.0983);
%             % ch1 (0-15 psig)
%             psi1(i,:) = (3*ch1(i,:)-0.074);
%             % ch2 (0-5 psig)
%             psi2(i,:) = (1*ch2(i,:)+0.0013);
%             % ch3 (0-15 psig)
%             psi3(i,:) = (3*ch3(i,:)-0.074);
%             % ch4
%             psi4(i,:) = (130.47*ch4(i,:)+4.1838);
%             % ch5
%             psi5(i,:) = (189.44*ch5(i,:)-0.1729);
%             % ch6 (0-15 psig)
%             psi6(i,:) = (3*ch6(i,:)-0.074);
%             % ch7 (0-5 psig)
%             psi7(i,:) = (1*ch7(i,:)+0.0013);
%         end
```

Figure A.2: MATLAB script used to pre-process experimental data (see chapter 2). This is part 2 of 5.

```
    % 45 degrees
%         for i = 1:length(ch4)
%             % ch0 (0-30 psig)
%             psi0(i,:) = (6.0216*ch0(i,:)-0.0983);
%             % ch1 (0-15 psig)
%             psi1(i,:) = (3*ch1(i,:)-0.074);
%             % ch2 (0-5 psig)
%             psi2(i,:) = (1*ch2(i,:)+0.0013);
%             % ch3 (0-15 psig)
%             psi3(i,:) = (3*ch3(i,:)-0.074);
%             % ch4
%             psi4(i,:) = (130.75*ch4(i,:)+4.2202);
%             % ch5
%             psi5(i,:) = (183.79*ch5(i,:)-0.1617);
%             % ch6 (0-15 psig)
%             psi6(i,:) = (3*ch6(i,:)-0.074);
%             % ch7 (0-5 psig)
%             psi7(i,:) = (1*ch7(i,:)+0.0013);
%         end
    % 90 degrees
%         for i = 1:length(ch4)
%             % ch0 (0-30 psig)
%             psi0(i,:) = (6.0216*ch0(i,:)-0.0983);
%             % ch1 (0-15 psig)
%             psi1(i,:) = (3*ch1(i,:)-0.074);
%             % ch2 (0-5 psig)
%             psi2(i,:) = (1*ch2(i,:)+0.0013);
%             % ch3 (0-15 psig)
%             psi3(i,:) = (3*ch3(i,:)-0.074);
%             % ch4
%             psi4(i,:) = (130.55*ch4(i,:)+4.2122);
%             % ch5
%             psi5(i,:) = (185.2*ch5(i,:)-0.1939);
%             % ch6 (0-15 psig)
%             psi6(i,:) = (3*ch6(i,:)-0.074);
%             % ch7 (0-5 psig)
%             psi7(i,:) = (1*ch7(i,:)+0.0013);
%         end
```

Figure A.3: MATLAB script used to pre-process experimental data (see chapter 2). This is part 3 of 5.

```
    % 135 degrees
%         for i = 1:length(ch4)
%             % ch0 (0-30 psig)
%             psi0(i,:) = (6.0216*ch0(i,:)-0.0983);
%             % ch1 (0-15 psig)
%             psi1(i,:) = (3*ch1(i,:)-0.074);
%             % ch2 (0-5 psig)
%             psi2(i,:) = (1*ch2(i,:)+0.0013);
%             % ch3 (0-15 psig)
%             psi3(i,:) = (3*ch3(i,:)-0.074);
%             % ch4
%             psi4(i,:) = (130.37*ch4(i,:)+4.2166);
%             % ch5
%             psi5(i,:) = (185.42*ch5(i,:)-0.2039);
%             % ch6 (0-15 psig)
%             psi6(i,:) = (3*ch6(i,:)-0.074);
%             % ch7 (0-5 psig)
%             psi7(i,:) = (1*ch7(i,:)+0.0013);
%         end
    % 180 degrees
        for i = 1:length(ch4)
            % ch0 (0-30 psig)
            psi0(i,:) = (6.0216*ch0(i,:)-0.0983);
            % ch1 (0-15 psig)
            psi1(i,:) = (3*ch1(i,:)-0.074);
            % ch2 (0-5 psig)
            psi2(i,:) = (1*ch2(i,:)+0.0013);
            % ch3 (0-15 psig)
            psi3(i,:) = (3*ch3(i,:)-0.074);
            % ch4
            psi4(i,:) = (130.47*ch4(i,:)+4.1838);
            % ch5
            psi5(i,:) = (189.44*ch5(i,:)-0.1729);
            % ch6 (0-15 psig)
            psi6(i,:) = (3*ch6(i,:)-0.074);
            % ch7 (0-5 psig)
            psi7(i,:) = (1*ch7(i,:)+0.0013);
        end

% Define filename for output and write output to that file
fileNameOutput = strcat('E:\Natalie_Experimental\050714\',tlinel,'\InstPressure_psi.txt');
fid4 = fopen(fileNameOutput,'at');
```

Figure A.4: MATLAB script used to pre-process experimental data (see chapter 2). This is part 4 of 5.

```
% Store each channel in a matrix called scA1
    % Print the scA1 matrix to the specified output file
    fprintf(fid4,'  ch0[psi]    ch1[psi]    ch2[psi]    ch3[psi]    ch4[psi]    ch5[psi]    ch6[psi]    ch7[psi
    for p = 1:length(ch4)
         scA1=[psi0(p,:) psi1(p,:) psi2(p,:) psi3(p,:) psi4(p,:) psi5(p,:) psi6(p,:) psi7(p,:)];
         fprintf(fid4,' %+5.3E' ,scA1);
         fprintf(fid4,'\n');
    end

    % Close the current output file
    fclose(fid4);
    tline1 = fgetl(fid1);

end

fclose(fid1);
```

Figure A.5: MATLAB script used to pre-process experimental data (see chapter 2). This is part 5 of 5.

```
%%%%%%%%%%%%%%%%%%%%%%%%data_preprocess_91CFD.m%%%%%%%%%%%%%%%%%%%%%%%%%%%%%%
read_path='F:\CFD\91m_Output\Tables\pv\axcenterline\'; % path to all of the data files
read_file_prefix = 'Axial_Centerline_table_';
read_file_prefix = strcat(read_path,read_file_prefix);

data_destination = 'converted_data\'; % converted file destination folder name
write_path = strcat(read_path,data_destination);
mkdir(write_path);

% Number of Files
nf = 1053; % number of files being extracted
%TS_0 = 2491000; %initial times step (warning: keep as a 7 digit integer)
TS_0 = 3000000;
dt = 1000000; %spacing between time steps (warning: pay attention to sig figs)
data_type = 'a'; % a for axial (normal to z), l for lateral, x for axial (normal to x)


for x = 0:nf

    TimeStep = (TS_0 - dt) + (x*dt);
    before = floor(TimeStep/1000000);
    after = TimeStep - (before*1000000);
    before = int2str(before);
    after = int2str(after);

    read_file = strcat(read_file_prefix,before,'.',after,'e+00.csv')

    % Read in the csv files
    M = csvread(read_file,1);

    % New matrix containing wanted and organized data
    if (data_type == 'l')
        new_matrix = [M(:,7),M(:,9),M(:,3),M(:,5)];
    elseif (data_type == 'a')
        new_matrix = [M(:,7),M(:,8),M(:,3),M(:,4)];
    elseif (data_type == 'x')
        new_matrix = [M(:,9),M(:,8),M(:,5),M(:,4)];
    end


    % Write matrix L to a tab delimited text file
    write_file = strcat(write_path,int2str(TimeStep),'.txt');
    dlmwrite(write_file,new_matrix,'delimiter','\t','precision','%10.6f');

end
```

Figure A.6: MATLAB script used to pre-process the velocity vector data from CFD (see chapter 6). This script was necessary to convert .csv files to .txt files that can be read by the PTV program and used in further data analysis. This script reads in the data and selects the columns of interest which are two direction columns and two vector columns corresponding to the directions of interest. The for loop allows the same code to be used for axial and lateral planes. The new file is saved as a text file.

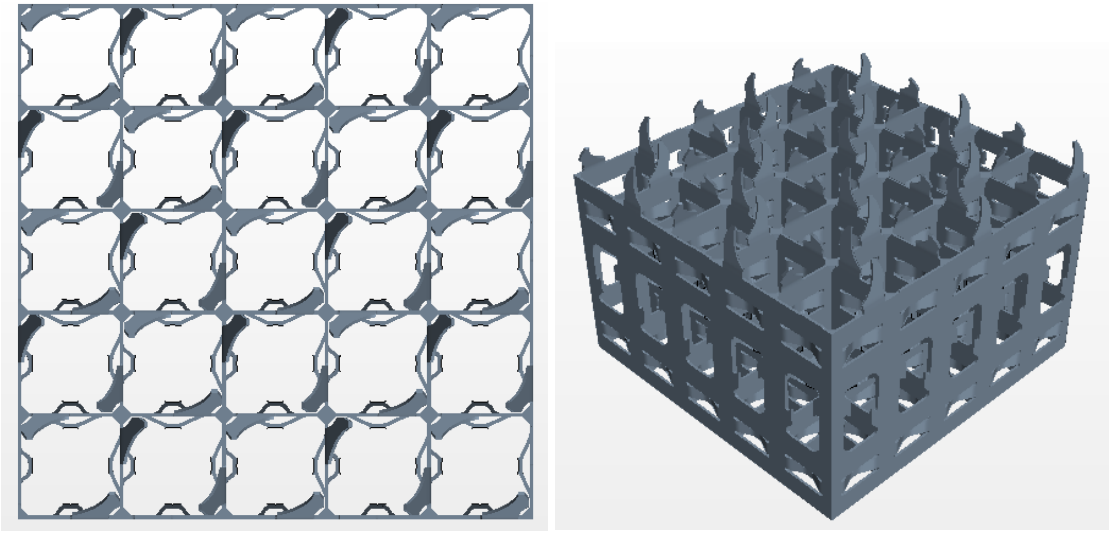

Figure A.7: Pictures of the V5H grid. Left is the top down view and right is the isometric view.

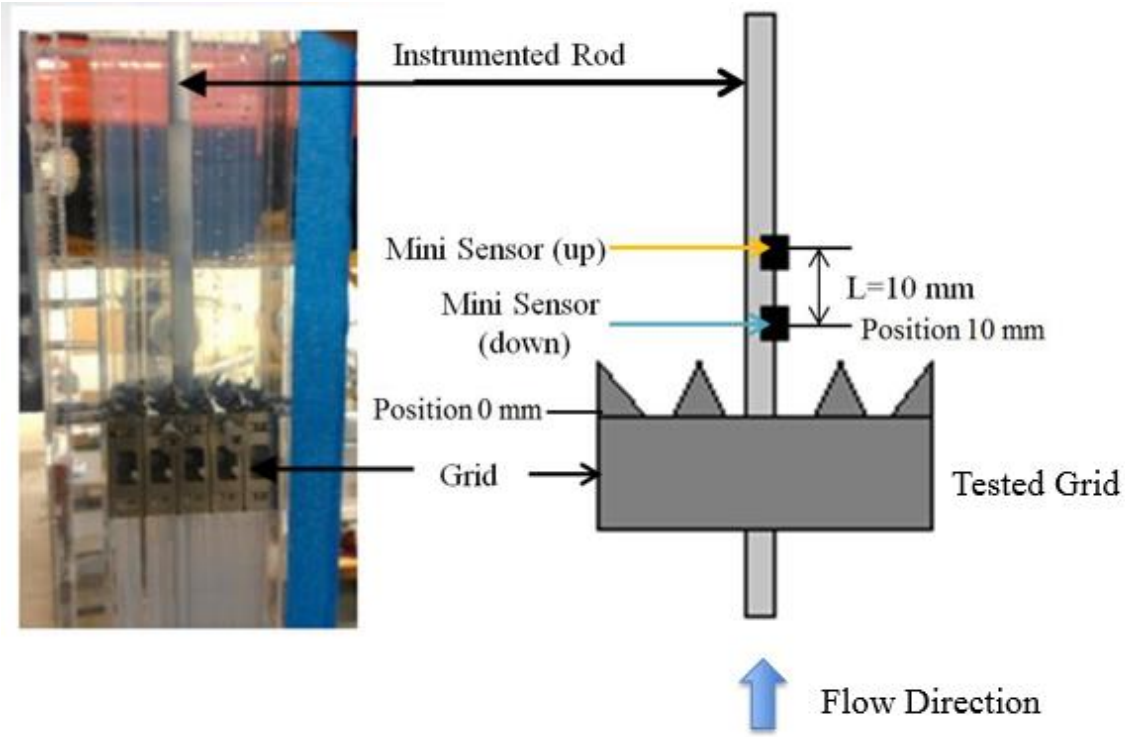

Figure A.8: Schematic of pressure transducer relative positon. Due to hardware issues, only the "down" sensor was used in this analysis.

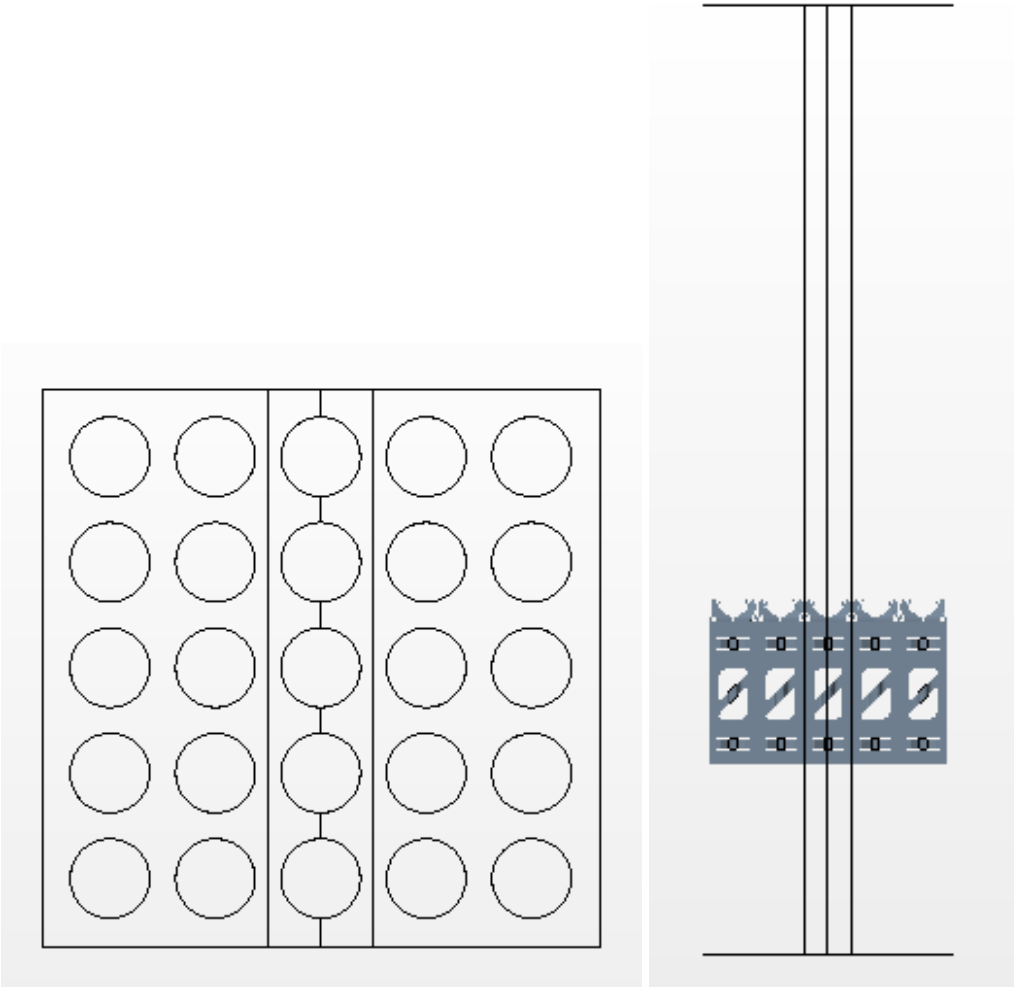

Figure A.9: Locations of the axial planes relative to the 5 x 5 rod bundle. Left is the top down view showing the planes relative location within the cross section of the bundle and right shows that the axial planes cover the entire axial domain of the simulation.

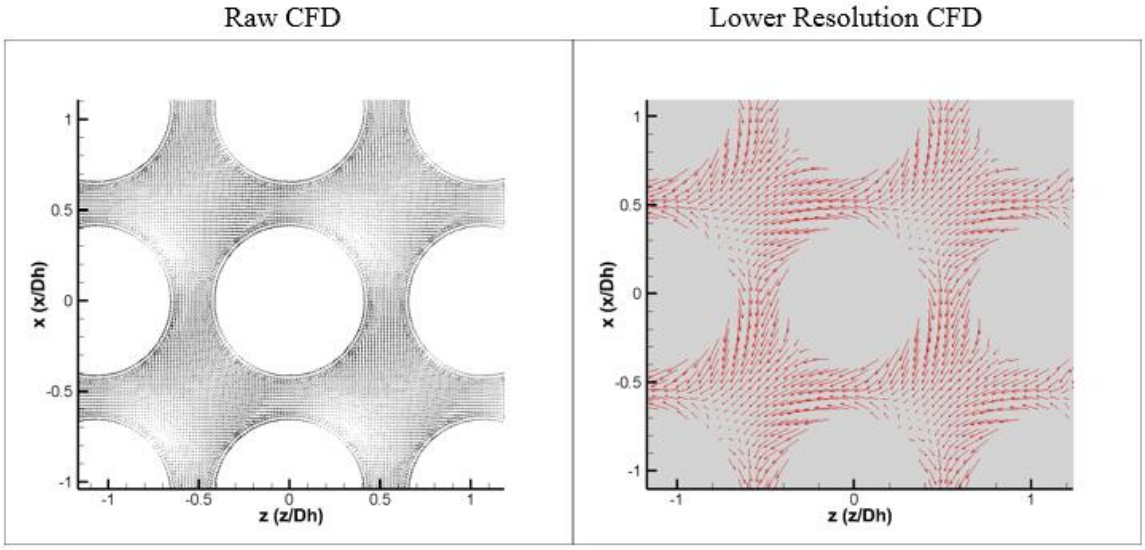

Figure A.10: Comparison between raw CFD vector resolution and the lower resolution achieved when velocity vectors from CFD were filtered using the PTV program. The lower resolution is easier for the reader to identify flow structures. Lower resolution plots of CFD velocity vectors will be used to compare directly with PIV data using the same resolution.

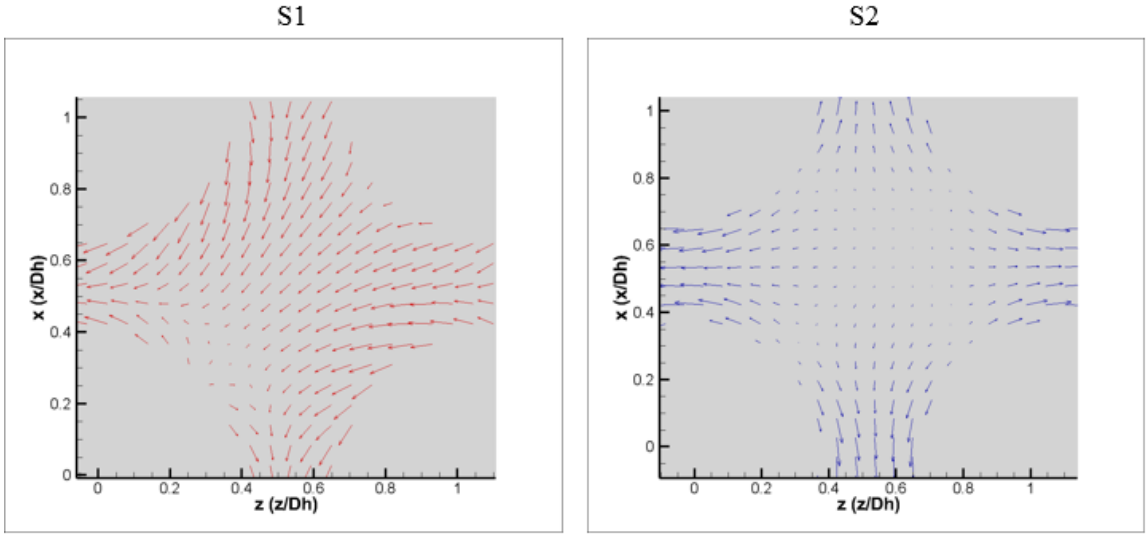

Figure A.11: One subchannel comparison of S1 and S2 velocity vectors one hydraulic diameter upstream of the mixing grid. These results are for subchannel 7. As expected at this elevation, there are no vortices present. The vortices are caused by the mixing vanes which the flow has not seen at this point.

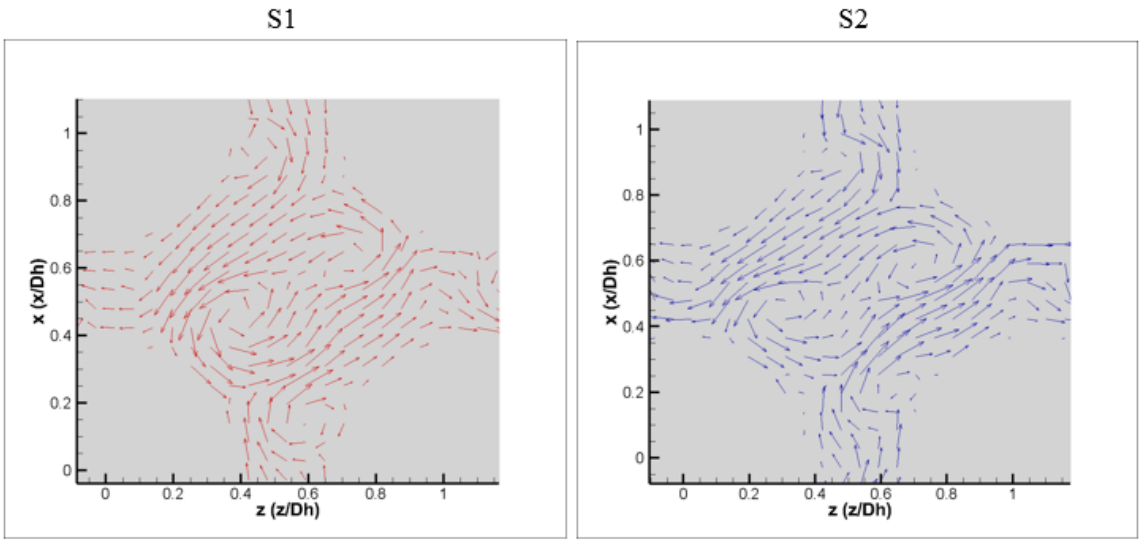

Figure A.12: One subchannel comparison of S1 and S2 velocity vectors 17 mm downstream of the mixing grid. These results are for subchannel 7. As expected four vortices can be seen in S1 and S2. The two big vortices in the center of the subchannel are due to the vanes and the two small ones closer to the gap region (area between subchannels) are created by the knee of the mixing vane.

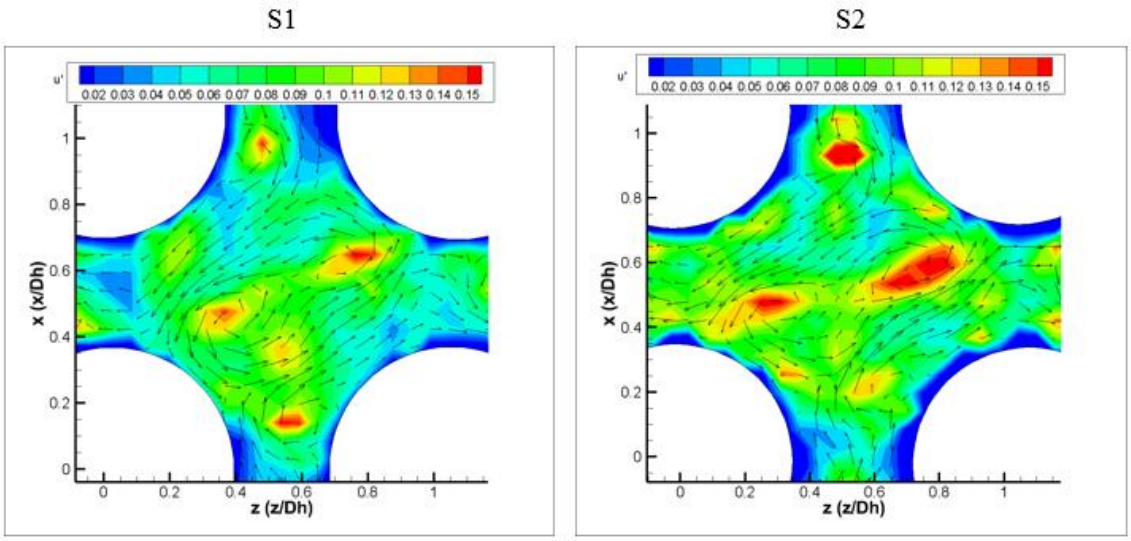

Figure A.13: One subchannel comparison of S1 and S2 velocity fluctuations in the axial direction (u') 17 mm downstream of the mixing grid. These results are for subchannel 7. In this plot it is evident that there are higher fluctuations present for S2 than S1.

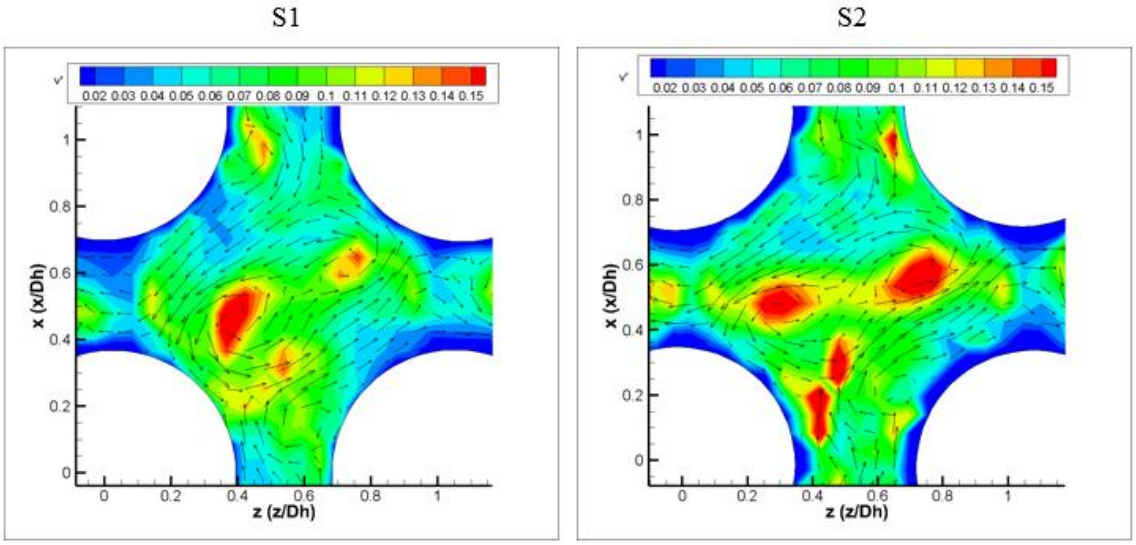

Figure A.14: One subchannel comparison of S1 and S2 velocity fluctuations in the x lateral direction (v') 17 mm downstream of the mixing grid. These results are for subchannel 7. In this plot it is evident that there are higher fluctuations present for S2 than S1.

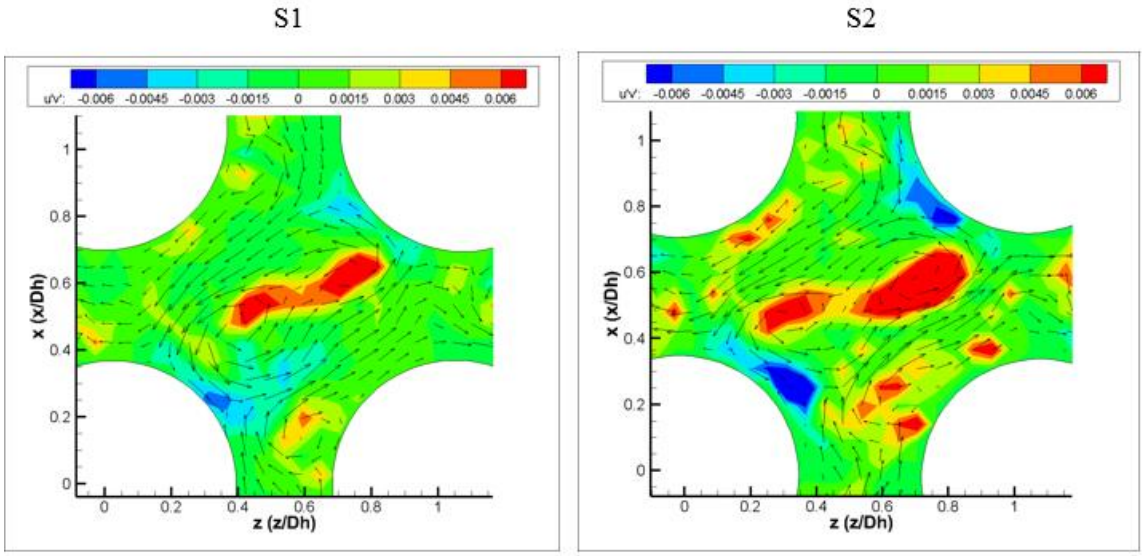

Figure A.15: One subchannel comparison of S1 and S2 Reynolds stress (u'v') 17 mm downstream of the mixing grid. These results are for subchannel 7. In this plot it is evident that there is higher Reynolds stress present for S2 than S1.

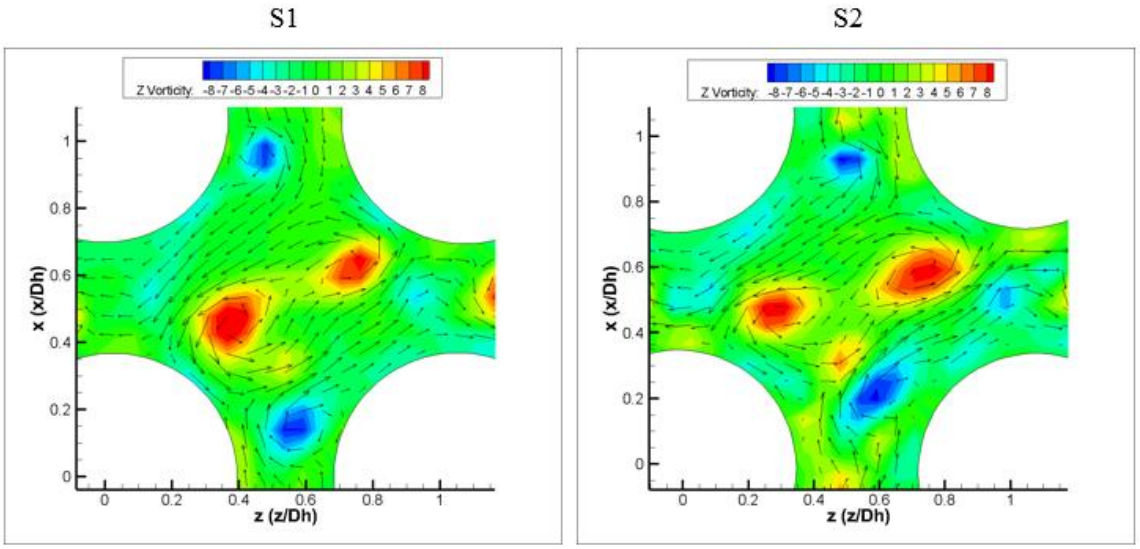

Figure A.16: One subchannel comparison of S1 and S2 Z vorticity 17 mm downstream of the mixing grid. These results are for subchannel 7. In this plot it is evident that there is higher vorticity present for S2 than S1. Also, more vortices smaller vortices are present in S2 than S1. The four vortices that are expected at this elevation are clearly present in both simulations. Plots of Z-vorticity are the clearest way to visualize the number of vortices.

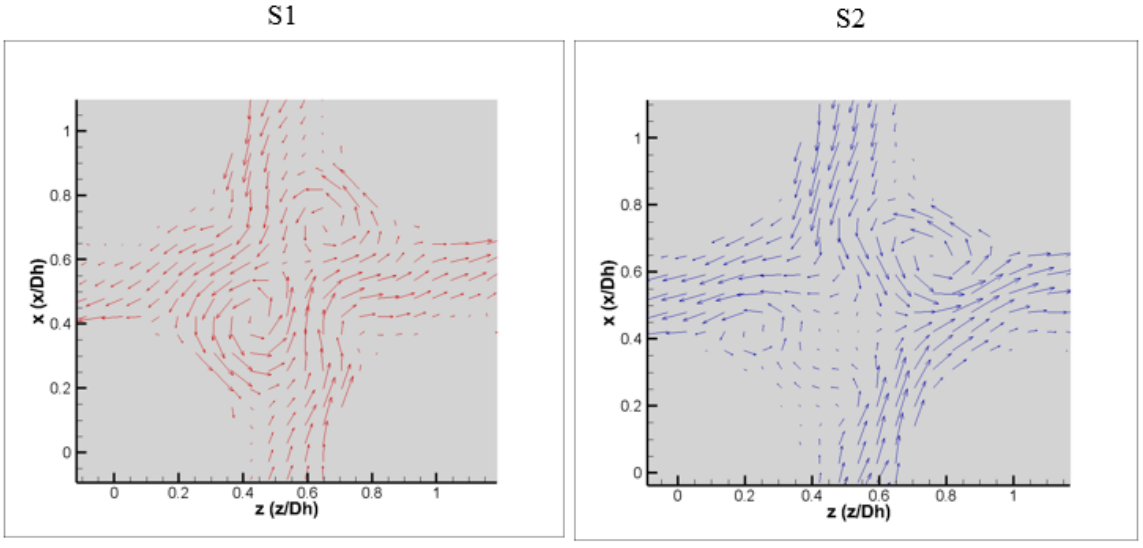

Figure A.17: One subchannel comparison of S1 and S2 velocity vectors 33 mm downstream of the mixing grid. These results are for subchannel 7. As expected, there are two visible vortices for S1 and S2. The difference is that S1 has circular vortices and S2 has elliptic vortices that are not as symmetric as S1.

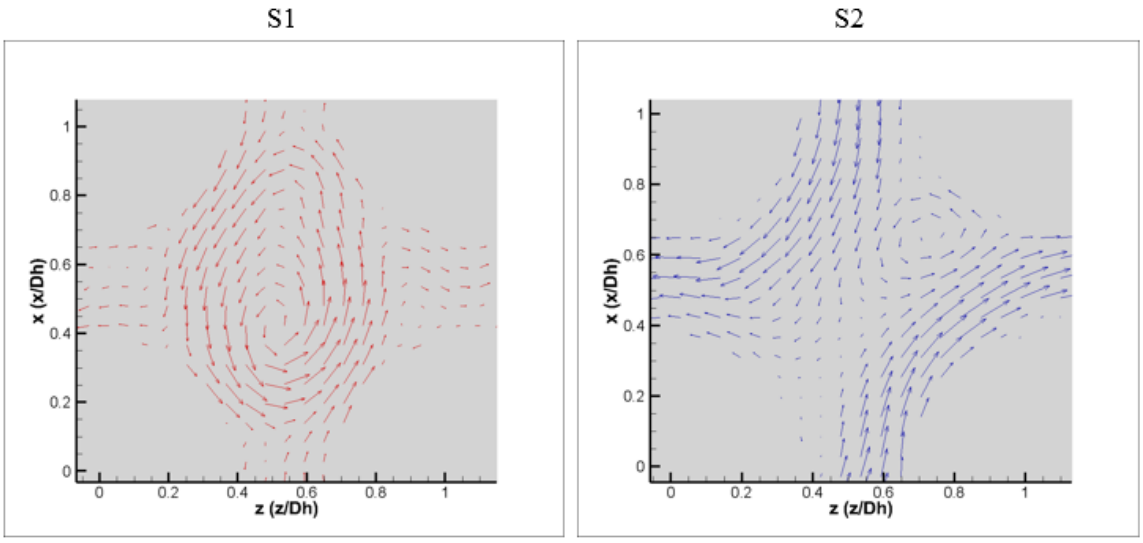

Figure A.18: One subchannel comparison of S1 and S2 velocity vectors 50 mm downstream of the mixing grid. These results are for subchannel 7. This axial elevation is expected to be the point of transition from two vortices per subchannel to one. In any given time step S1 will show one or two vortices where S2 mainly shows one on average. Another difference is that the vortices in S1 are generally centered within the subchannel and the S2 vortex is in a corner of the subchannel.

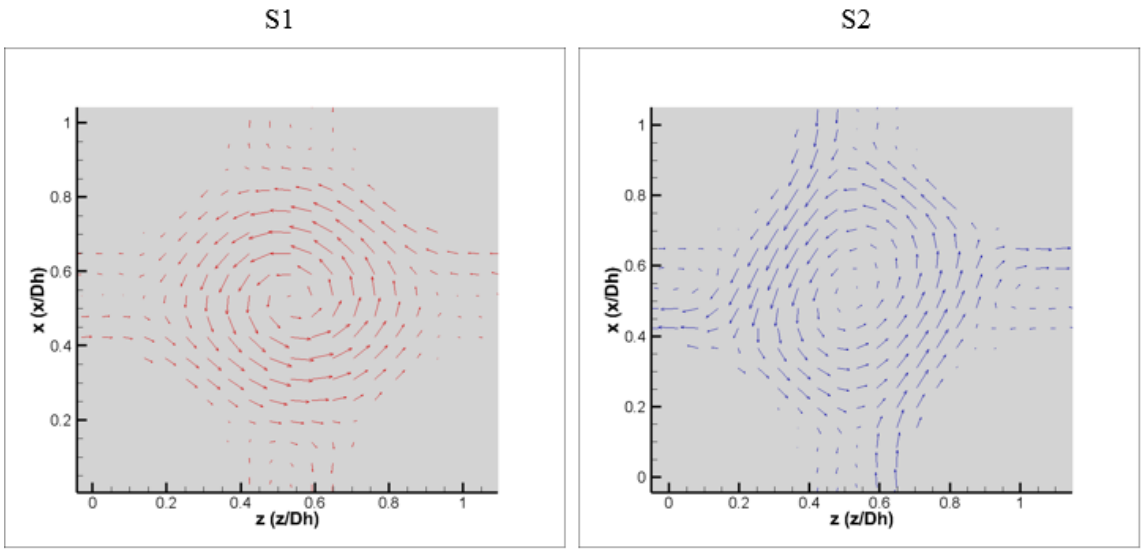

Figure A.19: One subchannel comparison of S1 and S2 velocity vectors 110 mm downstream of the mixing grid. These results are for subchannel 7. As expected, both simulations show a large vortex that occupies the entire subchannel.

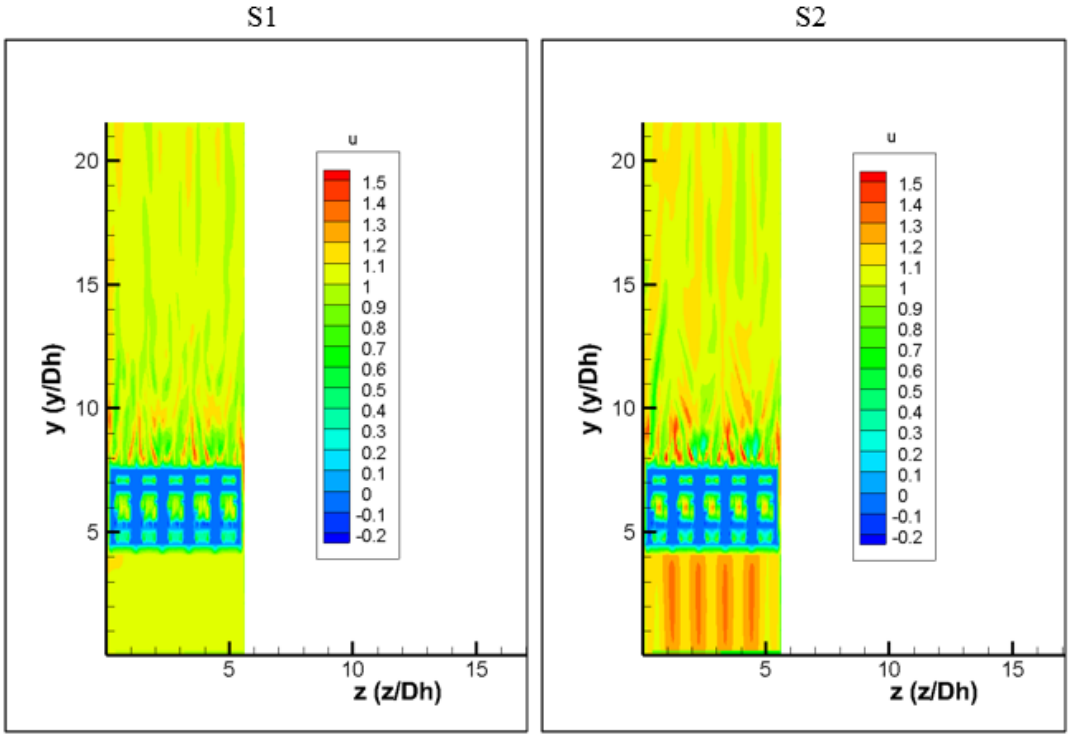

Figure A.20: Plot of axial velocity magnitude (u) at an axial plane in one of the central subchannels. A higher velocity was observed in S2 compared to S1 despite the mean inlet velocity being approximately the same.

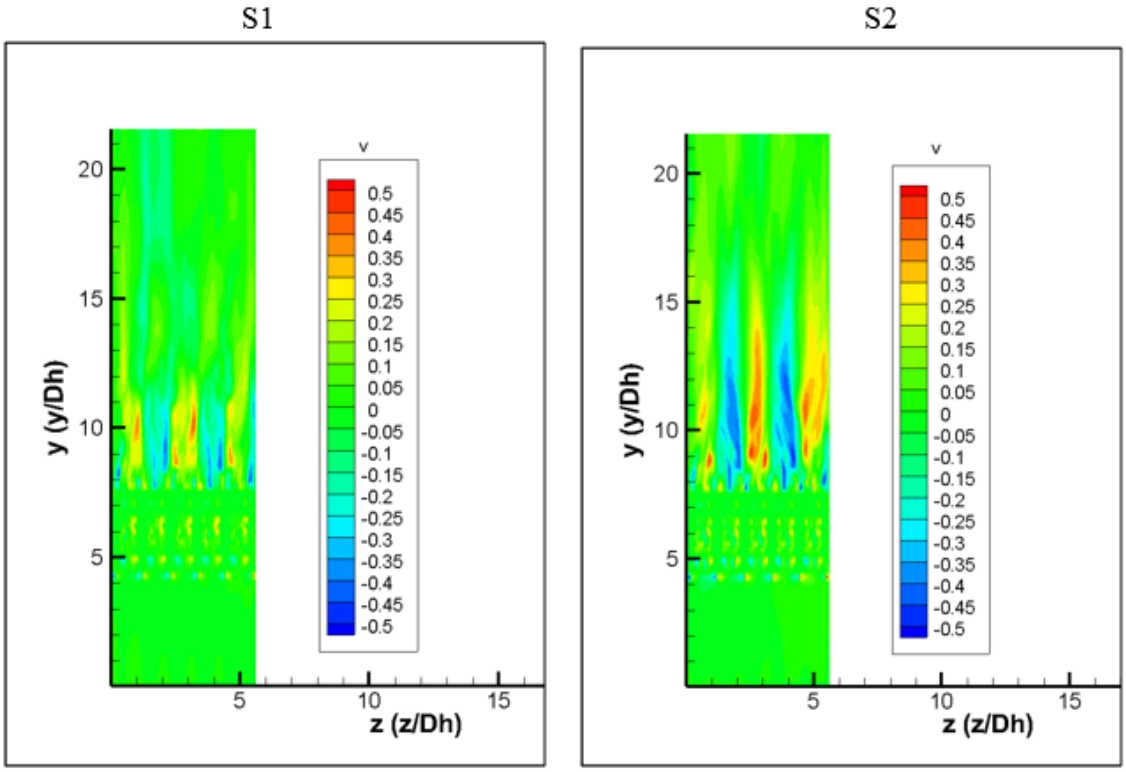

Figure A.21: Plot of lateral velocity magnitude (v) at an axial plane in one of the central subchannels. A higher velocity was observed in S2 compared to S1 despite the mean inlet velocity being approximately the same. This also means there is additional cross flow in S2 than S1.

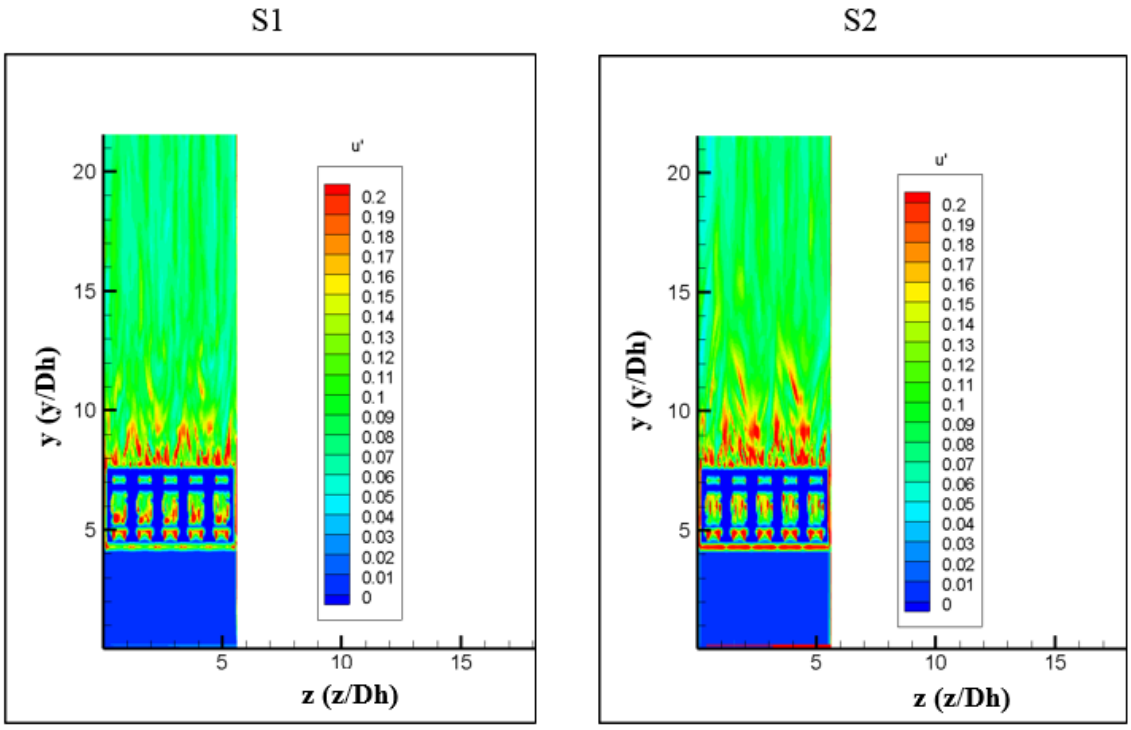

Figure A.22: Plot of axial velocity fluctuations (u') at an axial plane in one of the central subchannels. Higher velocity fluctuations were observed in S2 compared to S1 despite the mean inlet velocity being approximately the same.

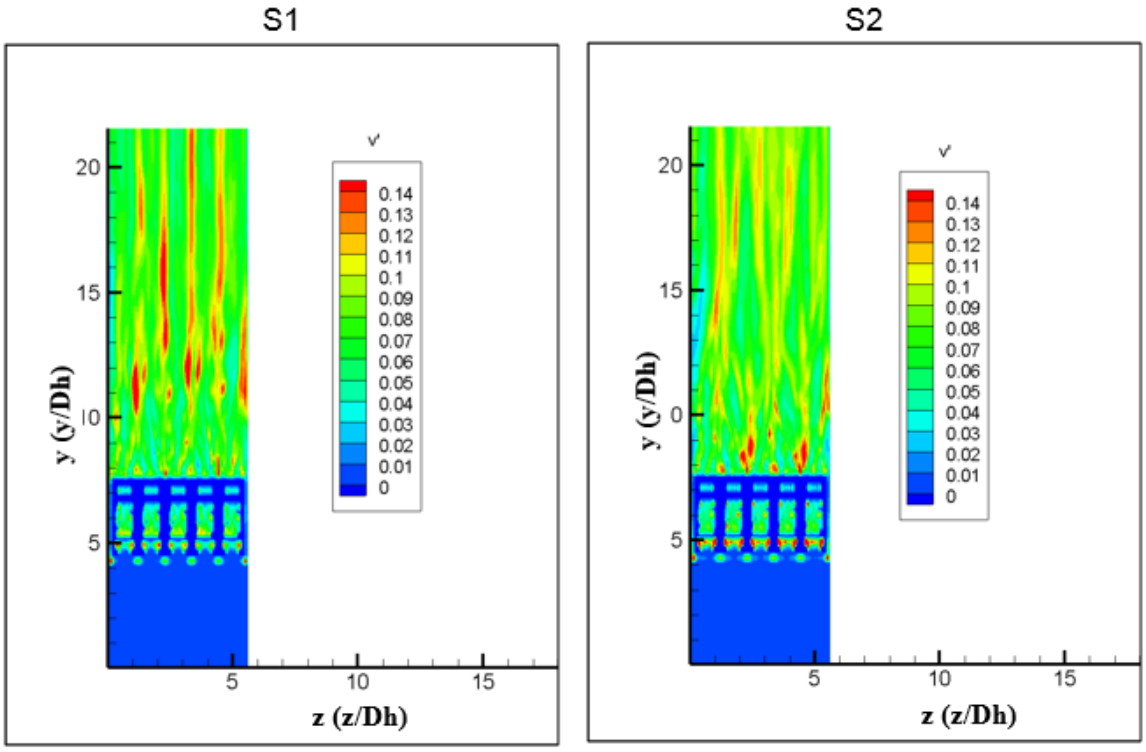

Figure A.23: Plot of lateral x velocity fluctuations (v') at an axial plane in one of the central subchannels. Higher velocity fluctuations were observed in S2 near the grid, but S1 has higher fluctuations further downstream.

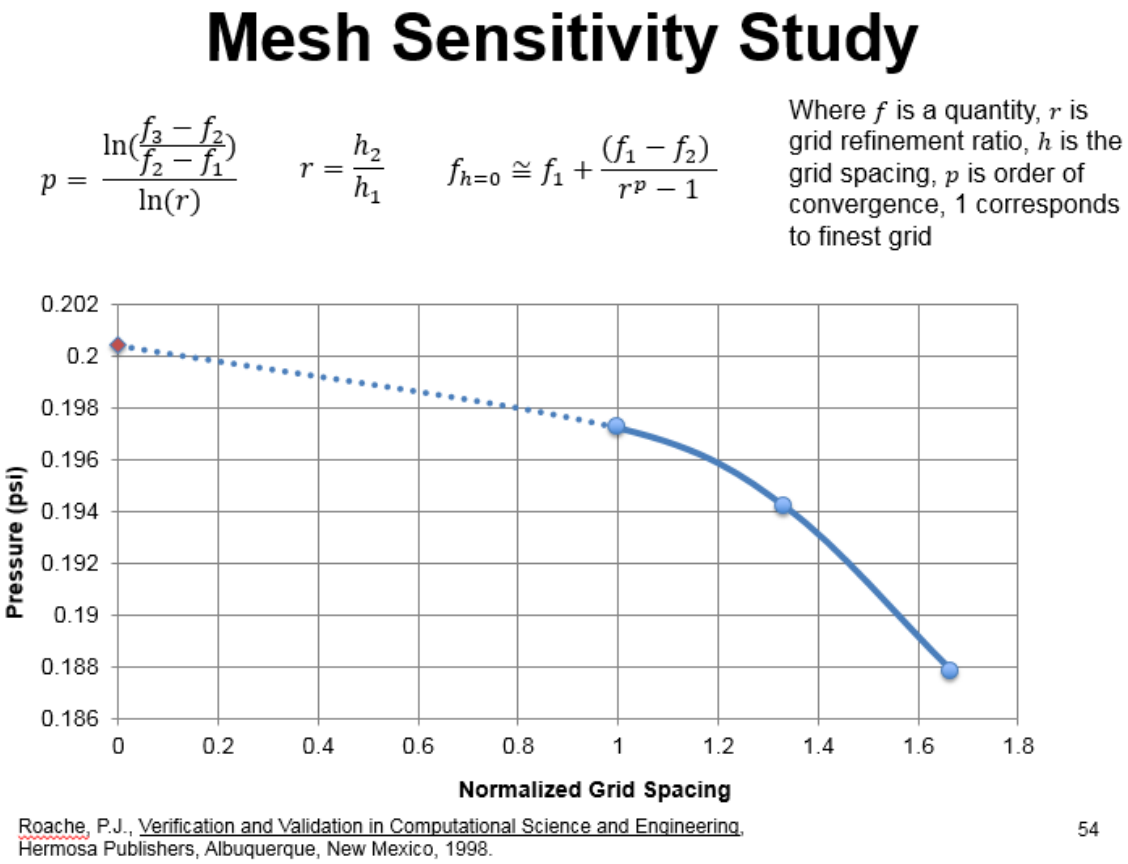

Figure A.24: The specifics of the mesh sensitivity study are given in this figure. The equations used can be found in the work by Roache and is reference number 20.

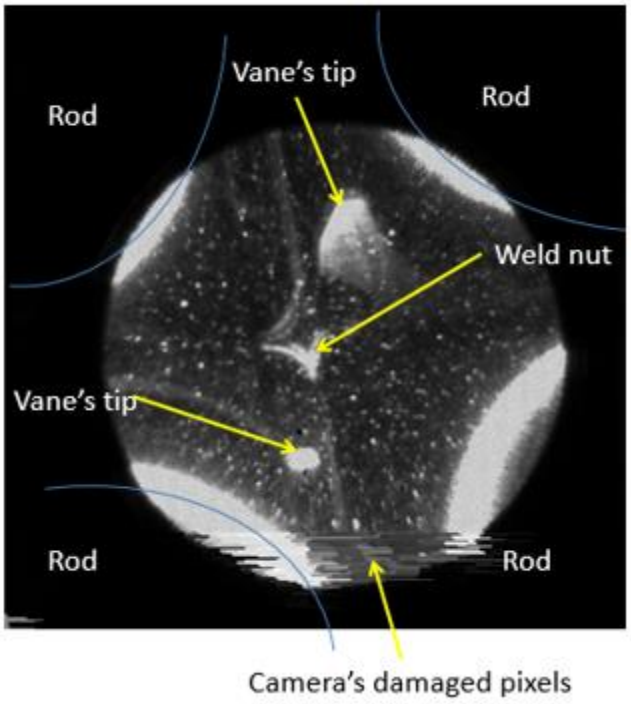

Figure A.25: Example of PIV data that will be compared to the CFD flow schemes in a future analysis.

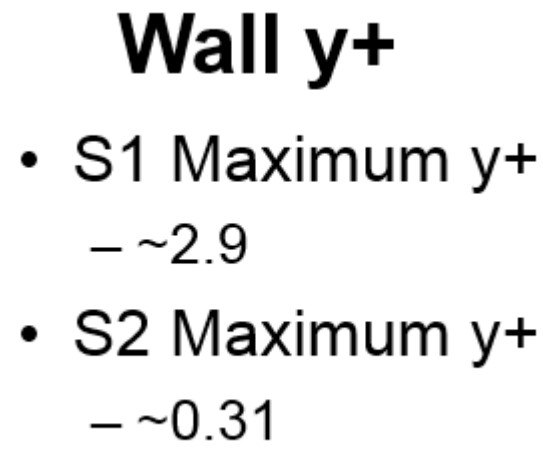

Figure A.26: Wall y+ values for S1 and S2 respectively.